



Four-dimensional variational inversion of black carbon emissions during ARCTAS-CARB with WRFDA-Chem

Jonathan J. Guerrette and Daven K. Henze

Department of Mechanical Engineering, University of Colorado, Boulder, CO 80309, USA

Correspondence to: Jonathan J. Guerrette (jonathan.guerrette@colorado.edu)

Received: 1 July 2016 – Discussion started: 17 October 2016

Revised: 24 March 2017 – Accepted: 22 April 2017 – Published: 22 June 2017

Abstract. Biomass burning emissions of atmospheric aerosols, including black carbon, are growing due to increased global drought, and comprise a large source of uncertainty in regional climate and air quality studies. We develop and apply new incremental four-dimensional variational (4D-Var) capabilities in WRFDA-Chem to find optimal spatially and temporally distributed biomass burning (BB) and anthropogenic black carbon (BC) aerosol emissions. The constraints are provided by aircraft BC concentrations from the Arctic Research of the Composition of the Troposphere from Aircraft and Satellites in collaboration with the California Air Resources Board (ARCTAS-CARB) field campaign and surface BC concentrations from the Interagency Monitoring of PROtected Visual Environment (IMPROVE) network on 22, 23, and 24 June 2008. We consider three BB inventories, including Fire INventory from NCAR (FINN) v1.0 and v1.5 and Quick Fire Emissions Database (QFED) v2.4r8. On 22 June, aircraft observations are able to reduce the spread between a customized QFED inventory and FINNv1.0 from a factor of 3.5 ($\times 3.5$) to only $\times 2.1$. On 23 and 24 June, the spread is reduced from $\times 3.4$ to $\times 1.4$. The posterior corrections to emissions are heterogeneous in time and space, and exhibit similar spatial patterns of sign for both inventories. The posterior diurnal BB patterns indicate that multiple daily emission peaks might be warranted in specific regions of California. The US EPA's 2005 National Emissions Inventory (NEI05) is used as the anthropogenic prior. On 23 and 24 June, the coastal California posterior is reduced by $\times 2$, where highway sources dominate, while inland sources are increased near Barstow by $\times 5$. Relative BB emission variances are reduced from the prior by up to 35 % in grid cells close to aircraft flight paths and by up to 60 % for fires near surface measurements. Anthropogenic variance reduc-

tion is as high as 40 % and is similarly limited to sources close to observations. We find that the 22 June aircraft observations are able to constrain approximately 14 degrees of freedom of signal (DOF), while surface and aircraft observations together on 23/24 June constrain 23 DOF. Improving hourly- to daily-scale concentration predictions of BC and other aerosols during BB events will require more comprehensive and/or targeted measurements and a more complete accounting of sources of error besides the emissions.

1 Introduction

Black carbon (BC) makes significant contributions to short-term climate (Bond et al., 2013) and human health (Janssen et al., 2012) as a component of aerosolized fine particulate matter ($PM_{2.5}$) in the atmosphere. BC is emitted through incomplete combustion from natural and anthropogenic burning of biomass and fossil fuels. Open biomass burning (BB), which includes natural wildfires, deforestation, and agricultural waste and prescribed burning, accounts for 40 % of total global BC emissions, while anthropogenic energy related sources (e.g., on- and off-road diesel and gasoline engines, industrial coal, residential cooking and heating) make up the remaining 60 % (Bond et al., 2013). Future climate conditions that increase drought and fire prevalence (e.g., Spracklen et al., 2009) and increasingly regulated anthropogenic sources might lead to a reversal of these ratios in California (Mao et al., 2011) and globally (Jolly et al., 2015). In California, BB events have been shown to increase surface $PM_{2.5}$ concentrations by a factor of 3 to 5 ($\times 3$ to $\times 5$), compared to non-fire periods (Wu et al., 2006). The heterogeneity

in BC emission and loss patterns and difficulty in replicating transport contribute to prediction uncertainty.

Despite the recognized importance of biomass emissions, large discrepancies remain in inventories in terms of biomass consumed and emitted chemical species. Fu et al. (2012) considered two different inventories during January and April 2006 over Southeast and East Asia, where the total emitted organic carbon (OC) and BC throughout the month differed by $\times 12$. F. Zhang et al. (2014) found similar variability between seven inventories in Africa during February 2010. F. Zhang et al. (2014) concluded that diffusion and loss mechanisms limit the corresponding responses of domain-wide aerosol burden, AOD, and 2 m temperature to $\times 2$ –3. However, the inventory spread for larger source magnitudes led to modeled column burden spreads of $\times 16$ –30 at hourly to daily grid scales.

The large range in inventories at fine scales results from the differing ways in which they are built. In order to be globally applicable, fire locating algorithms use remotely sensed hotspots from polar-orbiting satellites. Some provide additional regional locational and diurnal information with geostationary instruments. In all cases, daily emissions in a grid cell are calculated as the product of activity (kg burned) and emission factors for each species and vegetation class combination (kg emitted (kg burned)⁻¹). Bottom-up inventories combine rough estimates of burned area with vegetation densities and percent biomass burned associated with different land cover types (LCTs) to determine fire activity (e.g., Wiedinmyer et al., 2011; Reid et al., 2009; van der Werf et al., 2010). Top-down approaches use fire radiative power (FRP) measured by polar-orbiting or geostationary satellites and the LCT-specific energy content (e.g., Kaiser et al., 2012; Zhang et al., 2012), which circumvents using uncertain estimates of burned areas (Boschetti et al., 2004). A third approach combines the FRP with top-down constraints of aerosol optical depth (AOD) (e.g., Ichoku et al., 2012; Darmenov and da Silva, 2015). All three of these approaches cross reference fire locations with biome lookup tables to obtain the species-specific emission factors for each fire.

Improving short-term, local BC concentration predictions requires characterization of fine-scale spatial and diurnal patterns of BB emissions. The weakness of using only polar-orbiting data (e.g., Moderate Resolution Imaging Spectroradiometer (MODIS) instruments aboard Terra and Aqua) in bottom-up fire inventories is that there are nominally four overpasses per day, often with missed detections due to cloud and smoke cover or fire sizes beyond the instrument detection limits. Thus, these observations provide little information about the diurnal pattern of fire counts and FRP. Zhang et al. (2012) and Andela et al. (2015) devise methods for deriving climatological diurnal FRP patterns using geostationary observations. Both provide new information to modelers, but the former is not generalizable to grid-scale diurnal variability and the latter precludes the possibility that diurnal FRP (Zhang et al., 2012) and emissions (Saide et al., 2015)

patterns may be bimodal for specific LCTs and fire regimes, or due to local meteorology.

In contrast to their BB counterparts, anthropogenic emissions of BC are periodic across weekly and annual timescales. Their spatial distributions are relatively well known in developed countries, and less so in developing countries (Bond et al., 2013). Global estimates of annual anthropogenic BC emissions vary by $\times 2$ (Bond et al., 2013); national annual BC emissions in Asian countries and regions have uncertainties from $\times 2$ to $\times 5$ (Streets et al., 2003). In North America, including in California, uncertainties still persist in terms of characterizing the magnitude of emissions in a particular year, seasonal variability, and long-term trends in activity and control strategies (Grieshop et al., 2006; McDonald et al., 2015). Bond et al. (2013) cite several inventories of annual US non-BB BC sources, which are between 260 and 440 Ggyr⁻¹, yielding a maximum to minimum ratio of 1.7. However, like many other inventories, the US EPA National Emission Inventory (Reff et al., 2009) does not specify uncertainty bounds either for the whole country or at state and county levels.

These challenges in characterization of both BB and anthropogenic emissions of BC and co-emitted species have led to the proliferation of top-down constraint methods of varying complexity and utility. Several studies have used adjoint-free methods for anthropogenic emissions in Los Angeles, California, using aircraft measurements during the 2010 California Research at the Nexus of Air Quality and Climate Change (CalNex) campaign. Brioude et al. (2013) constrained CO, NO_x, and CO₂, and Cui et al. (2015) constrained CH₄; both applied a Lagrangian particle dispersion model (LPDM). Peischl et al. (2013) constrained CH₄ using a mass balance approach and light alkane signatures from multiple sectors. LPDM benefits from being able to resolve sources on as fine of a grid resolution as is used in the underlying model. Both LPDM and mass balance are limited to linear tracer problems where observations are recorded under specific meteorological conditions. Wecht et al. (2014) used GEOS-Chem in an analytical inversion to compare constraints from the CalNex aircraft measurements with those from present and future satellite observations of CH₄ throughout California. Although an analytical inversion does not require an adjoint, the approach is limited, computationally, to constraining only a few sources, which imposes aggregation error (Mao et al., 2015). Adjoint-based four-dimensional variational data assimilation (4D-Var) is able to account for nonlinear behavior between the emission sources and observation receptors by calculating exact gradients across physical processes. Such an approach does not have the limitations imposed by mass balance, LPDM, or analytical inversions, but does require development of an adjoint. The gradients are usually calculated through an adjoint model, although recent work (Saide et al., 2015) performs 4D-Var on a limited area fire without an adjoint. That new approach, while easier to implement, is limited to solving for

only a few spatially distributed sources due to computational limitations.

In this study, we adapt the adjoint-based incremental 4D-Var used in the WRFDA weather forecasting system (Barker et al., 2005; Huang et al., 2009) to solve tracer surface flux estimation problems. The modifications to that system that are required for this work are described in Sect. 2 as well as in Guerrette and Henze (2015) (GH15). These include new linearized model descriptions (GH15), memory and I/O trajectory management (GH15), a log-normal emission control variable (Sect. 2.3.2), calculation of posterior variance (Sect. 2.3.4), and improvements to the Gauss–Newton optimization algorithm to handle nonlinearities (Sect. 2.3.5). As described in GH15, this approach of assimilating chemical tracer observations in a regional numerical weather prediction and chemistry model is unique in the context of previous 4D-Var flux constraints.

We apply the resulting tool, WRFDA-Chem, to constrain anthropogenic and BB sources of BC throughout California during the Arctic Research of the Composition of the Troposphere from Aircraft and Satellites in collaboration with the California Air Resources Board (ARCTAS-CARB) field campaign. In June 2008, ARCTAS-CARB characterized aerosols and trace gases throughout California with DC-8 aircraft flights on 20 (Friday), 22 (Sunday), 24 (Tuesday), and 26 (Wednesday) June (Jacob et al., 2010). Sahu et al. (2012) used BC total mass measurements from a single-particle soot photometer (SP2) and other simultaneous gas-phase measurements to identify and characterize anthropogenic and BB plumes in California. By using these observations and surface measurements from every third day from the Interagency Monitoring of PROtected Visual Environment (IMPROVE) network (Malm et al., 1994), we provide top–down estimates of BC surface fluxes using 4D-Var. The mixture of anthropogenic and BB sources distributed across complex terrain and biomes is a difficult system to characterize. Still, this scenario is typical of daily smoke exposure forecasting during acute wildfire events, and is a relevant first test case for the new 4D-Var system.

The approach taken in this work is described in Sect. 2, including the forward, adjoint, and tangent linear models, the prior inventories and domain, and the adaptation of WRFDA. Section 3 describes the application of WRFDA-Chem to the BB and anthropogenic emission inversion problem during ARCTAS-CARB. We conclude with a summary and recommendations for future measurements and emission inversion research.

2 Method

2.1 Nonlinear, adjoint, and tangent linear models

Incremental 4D-Var requires forward nonlinear (NLM), adjoint (ADM), and tangent linear (TLM) models. The NLM is

nearly identical to WRF-Chem (Grell et al., 2005), with the addition of emissions scaling factors. The GOCART option facilitates 19 species, including 4 gas and aerosol species for sulfate chemistry, hydrophobic and hydrophilic BC and organic carbon, 5 size bins for dust, 4 bins for sea salt, and 2 diagnostic species for PM_{2.5} and PM₁₀. While we use GOCART, the results presented are limited to BC. The model configuration is the same as was used in Guerrette and Henze (2015), and is summarized as follows: ACM2 PBL mixing (Pleim, 2007a, b), the Pleim–Xiu land surface model (Xiu and Pleim, 2001; Pleim and Xiu, 2003; Pleim and Gilliam, 2009) and surface layer (Pleim, 2006) mechanisms without soil moisture and temperature nudging, Wesely dry deposition velocities (Wesely, 1989), GSFC shortwave and Goddard longwave radiation, and microphysics turned off. Microphysical and radiative responses to online aerosols are not taken into account for GOCART aerosols in WRF-Chem.

We utilize the recently developed WRFPLUS-Chem (Guerrette and Henze, 2015), which contains ADM and TLM code extending the original WRFPLUS software (Zhang et al., 2013). WRFPLUS-Chem describes chemical tracers in the context of planetary boundary layer (PBL) mixing, emissions, dry deposition, and GOCART aerosols. ADM and TLM gradients have been verified against finite difference approximations. Second-order checkpointing reduces the memory footprint to a feasible level for ADM and TLM simulations over longer durations (>~6 h) and/or that use many chemical tracers (>~10). Guerrette and Henze (2015) applied the ADM in calculating sensitivities relevant to the emission inversion carried out here. Section 3.5 includes a comparison of the results of that study with the posterior emissions here.

The model domain is similar to that used by Guerrette and Henze (2015). The spatial extent encompasses California and other southwestern US states. We conduct two emission inversions, the first on 22 June with a focus on biomass burning sources, and the second on 23–24 June with a focus on anthropogenic sources. We generated chemical initial conditions by running WRF-Chem from 15 June 2008, 00:00:00 up until the beginning of each inversion period. We used the default WRF-Chem boundary condition for a BC concentration of 0.02 µg kg⁻¹, which was found to be consistent with observations with an upwind flight on 22 June. Meteorological initial and boundary conditions are interpolated from 3 h, 32 km North American Regional Reanalysis (NARR) fields. The horizontal resolution is 18 km throughout 80 × 80 columns, and there are 42 vertical levels between the surface and model top at 100 hPa.

Our horizontal grid spacing was chosen to balance the wall-time and memory requirements of 4D-Var with model accuracy, and the ACM2 PBL option was chosen to reduce ADM and TLM development efforts. Angevine et al. (2012) recommend that the complex terrain in California demands fine tuning of the WRF horizontal grid spacing, PBL, LSM, and reanalysis initialization. Among other conclusions, those

authors found that at six surface sites near the land–ocean boundary, 4 and 12 km simulations with similar settings had mean wind speed biases of $(0.15 \text{ to } 1.5) \text{ m s}^{-1}$ and $(-0.38 \text{ to } 1.9) \text{ m s}^{-1}$, respectively. Supporting that conclusion, Strand et al. (2012) used a 36 km resolution chemical transport model (CTM), with offline meteorology, and found significant negative mean fractional bias (MFB) in modeled $\text{PM}_{2.5}$ relative to surface observations of fires within narrow northern California valleys in July 2008 (MFB = -34.95%) and during autumn 2007 Santa Ana winds (MFB = -110.22%). During the July 2008 episode, their CTM predictions had a smaller positive bias (MFB = $+21.88\%$). Therefore, we would expect similar wind and concentration biases at 18 km resolution, which may or may not be improved by online meteorology. Incremental 4D-Var provides an opportunity to utilize a different model configuration (e.g., resolution) for the NLM comparisons of model to observations than that used for the ADM and TLM simulations. The adaptation of that capability from meteorological (i.e., X. Zhang et al., 2014) to chemical simulations and the subsequent testing is reserved for future WRFDA-Chem developments.

2.2 Prior emission inventories

The prior includes sources of BC from anthropogenic activity and natural wildfires. Anthropogenic emissions are taken from the US EPA's 2005 National Emissions Inventory (NEI05) for mobile and point sources, including for example diesel on-road and power production from coal. The individual sectors are lumped together for each grid cell. We represent BB emissions using three different wildfire inventories, FINNv1.0 and v1.5, both at $1 \text{ km} \times 1 \text{ km}$ resolution (Wiedinmyer et al., 2011, 2006), and QFEDv2.4r8 at $0.1^\circ \times 0.1^\circ$ resolution (Darmenov and da Silva, 2015). FINNv1.5 is readily available through NCAR (<http://bai.acom.ucar.edu/Data/fire/>) to WRF-Chem users, while FINNv1.0 is no longer supported. However, we include FINNv1.0 in this study, because it shows the equivalent value as a prior. FINN and QFED fall into the first (bottom–up) and third (top–down constraint with AOD) categories of BB inventories described in Sect. 1, respectively.

Any inverse modeling study that depends on an initial guess should start in a region of high probability. In a Bayesian inversion, the first guess should be unbiased. Here we address several known errors in our prior inventories that we either fix or are unable to fix. All changes are consistent with either observations or the intended physical descriptions of the inventories.

QFED scales global aerosol emissions from four biome types through multiple linear regression between observed MODIS aerosol optical depth (AOD) and modeled GEOS-5 AOD during the years 2004–2009. For temperate forests QFED scales aerosols by $\times 4.5$ throughout the world. That vegetation category accounts for 80% of the wildfire BC in California during 22–30 June 2008. The global scaling

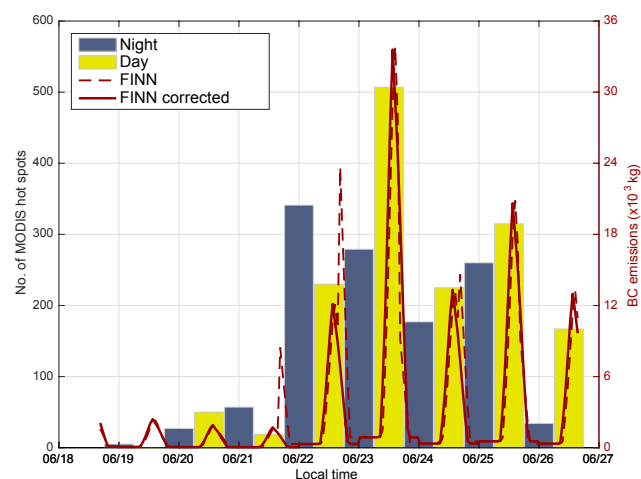


Figure 1. MODIS fire hotspot detections, excluding those with confidence less than or equal to 20% and double detections within 1.2 km of each other (left axis) and domain-wide FINNv1.0 BB emissions during the ARCTAS-CARB campaign, with and without fixes described in Sect. 2.2 (right axis).

is problematic for the California fires, because the GEOS-5 AOD is biased high in the western US during the summer fire seasons of 2006–2008 (Fig. C14 of Darmenov and da Silva, 2015). In order to match the regional climatological AOD scaling factors for the western US, we scale all QFED BC sources by $\times 1/3$. This scaling is already taken into account in the prior emissions shown in Sect. 3.3, and without it FINNv1.0 and QFED would differ by $\times 10$ during the ARCTAS-CARB campaign.

The WRF preprocessor distributed with the FINN inventory is used to distribute ASCII formatted lists of both FINN and QFED daily speciated fire emissions to hourly netcdf files readable by WRF. The diurnal profile follows the Western Regional Air Partnership profile – WRAP (2005) – and is defined by a flux peak from 13:00 to 14:00 Local Time (LT), and flat fluxes equal to 2.5% of the peak value between 19:00 and 09:00 LT. Through modeling experience, we found two bugs with how the FINN preprocessor interprets the WRAP profile and have fixed them for this case study. The total FINNv1.0 emissions across the model domain before and after fixing these bugs are plotted in Fig. 1 along with MODIS active fire counts (NASA, 2014). The first bug relates to how the time zone of a particular fire is calculated from longitude. The preprocessor converts a decimal longitude to integer time-zone bins; this allows a fire at 120.1° W to be an hour earlier in the diurnal profile than a fire at 119.9° W , even though they should be at nearly identical positions in the WRAP profile. Such behavior might apply to anthropogenic emissions, where cities near time-zone borders follow different daily cycles of activity, but not to natural activity related to the 15° per hour cycle of the Sun.

The second bug, and the one most visible in Fig. 1, is in the redistribution of UTC fire detections into LT emissions. MODIS Terra and Aqua overpass times are distributed around noon and midnight LT globally, with some adjustment as the image capture location moves farther from the Equator. The fire hotspots are detected on UTC days, and their emissions are profiled according to LT periods corresponding to the same UTC day as the detection. In California, where the LT is UTC minus 8 h, the noon overpass corresponds to 20:00 UTC, and 00:00 UTC corresponds to 16:00 LT on the previous day (Sun cycle). Therefore, when a fire is detected during nearly peak heat and emission fluxes at noon, a large fraction of the flux is apportioned to the previous afternoon. For locations east of the International Date Line, the LT reallocation is in the opposite direction. In either case, some portion of the profile is shifted by 24 h. This error is apparent as a temporal discontinuity in the case of transient fires that vary significantly in magnitude from one day to the next, especially after a recent ignition. Since the domain used here is nearly confined to a single time zone, we simply move the emissions forward 1 day for times between 16:00 and 23:00 LT (00:00–07:00 UTC). A more robust fix will need to be implemented in a future preprocessor.

Another error in the prior BB emissions is less easily resolved. Figure 2 shows where the MODIS active fires are located relative to the inventory fire locations. Since QFED fires are provided on a lat–lon grid, the fire centers do not coincide with its grid centers. When the inventory is distributed to the 18 km model grid, some emissions are shifted over by one column relative to the FINN locations. There are several additional spurious emission locations in QFED, where no active fires were detected on either 21 or 22 June. In a month long simulation, differences in fire gridding between several inventories can be averaged out. In the shorter-term inversions over California presented in Sect. 3, the locational differences do affect the results.

2.3 WRFDA-Chem inversion system

2.3.1 Incremental 4D-Var

The aim of data assimilation (DA) is to optimally combine uncertain observations with uncertain model predictions to provide an improved estimate of the state of a system than either gives alone. Here we apply incremental 4D-Var as first introduced by Courtier et al. (1994), utilizing the existing software architecture in WRFDA, and extended to accommodate positive definite emissions with large associated uncertainties (Sect. 2.3.2). In Appendix A, we show (similar to Lawless et al., 2005; Gratton et al., 2007; Tshimanga et al., 2008) that incremental 4D-Var is equivalent to a Gauss–Newton (GN) optimization, where a cost function,

$$\min_{\delta \mathbf{x}^k} J(\delta \mathbf{x}^k) = \frac{1}{2} \left[\delta \mathbf{x}^k + (\mathbf{x}^{k-1} - \mathbf{x}_b) \right]^\top \mathbf{B}^{-1}$$

$$\begin{aligned} & \left[\delta \mathbf{x}^k + (\mathbf{x}^{k-1} - \mathbf{x}_b) \right] \\ & + \frac{1}{2} \left(\mathbf{G}^{k-1} \delta \mathbf{x}^k - \mathbf{d}^{o,k-1} \right)^\top \mathbf{R}^{-1} \\ & \left(\mathbf{G}^{k-1} \delta \mathbf{x}^k - \mathbf{d}^{o,k-1} \right), \end{aligned} \quad (1)$$

is linearized around a current guess of a control variable vector (CV), $\mathbf{x} \in \mathbb{R}^n$, minimized, then relinearized, and so on. $\delta \mathbf{x}^k$ is the CV perturbation sought in the k th linearization. \mathbf{x}_b is the vector of prior CVs, \mathbf{B} is the background covariance matrix, and \mathbf{R} is the model–observation error covariance matrix. The nonlinear operator,

$$G(\mathbf{x}) = \begin{pmatrix} H_1(\mathbf{x}) \\ \vdots \\ H_i(\mathbf{x}) \\ \vdots \\ H_N(\mathbf{x}) \end{pmatrix}, \quad (2)$$

is composed of the model–observation operators, with each H_i mapping \mathbf{x} to observation time i . The measurements at each acquisition time, $y_i^o \in \mathbb{R}^{m_i}$, are expressed independently for N acquisition times by

$$\mathbf{y}^o = \left[y_1^{o\top}, \dots, y_N^{o\top} \right]^\top \in \mathbb{R}^m, \quad (3)$$

where $\sum_{i=1}^N m_i = m$. The o superscript denotes that \mathbf{y}^o are observations. $\mathbf{d}^{o,k-1}$ is the innovation between observations and model values in the previous linearization:

$$\mathbf{d}^{o,k-1} = \mathbf{y}^o - G(\mathbf{x}^{k-1}). \quad (4)$$

The linearized cost function is derived under the assumption that

$$G(\mathbf{x}^k + \delta \mathbf{x}) \approx G(\mathbf{x}) + \mathbf{G}^{k-1} \delta \mathbf{x}, \quad (5)$$

where $\mathbf{G} \in \mathbb{R}^{n \times m}$ is the Jacobian of G . The superscript on \mathbf{G}^{k-1} denotes that it is linearized around the state from the previous iteration, i.e.,

$$\mathbf{G}^{k-1} = \begin{pmatrix} \mathbf{H}_1|_{\mathbf{x}^{k-1}} \\ \vdots \\ \mathbf{H}_i|_{\mathbf{x}^{k-1}} \\ \vdots \\ \mathbf{H}_N|_{\mathbf{x}^{k-1}} \end{pmatrix}. \quad (6)$$

In an emission inversion for a single chemical species, $n = n_x n_y n_t = O(10^5 - 10^6)$, depending on the domain size and temporal aggregation of posterior emissions. Since the number of members in \mathbf{B} is equal to n^2 , finding its inverse is computationally unfeasible. To circumvent that challenge, Barker et al. (2004) implemented the control variable transform

(CVT) through a square root preconditioner (Lorenc, 1988), \mathbf{U} , in WRFDA. The increment is transformed as $\delta \mathbf{x}^k = \mathbf{U} \delta \mathbf{v}^k$, where $\mathbf{B} = \mathbf{U} \mathbf{U}^\top$, $\mathbf{U}^\top \mathbf{B}^{-1} \mathbf{U} = \mathbf{I}_n$, and $\mathbf{I}_n \in \mathbb{R}^{n \times n}$ is the identity matrix. The transformed minimization problem is

$$\min_{\delta \mathbf{v}^k} J(\delta \mathbf{v}^k) = \frac{1}{2} (\delta \mathbf{v}^k - \mathbf{d}^{b,k-1})^\top (\delta \mathbf{v}^k - \mathbf{d}^{b,k-1}) + \frac{1}{2} (\mathbf{G}^{k-1} \mathbf{U} \delta \mathbf{v}^k - \mathbf{d}^{o,k-1})^\top \mathbf{R}^{-1} (\mathbf{G}^{k-1} \mathbf{U} \delta \mathbf{v}^k - \mathbf{d}^{o,k-1}), \quad (7)$$

where the background departure, summed over all previous outer iterations, is

$$\mathbf{d}^{b,k-1} = - \sum_{k_o=1}^{k-1} \delta \mathbf{v}^{k_o}. \quad (8)$$

In addition to circumventing the calculation of \mathbf{B}^{-1} , the preconditioner reduces the condition number of the problem, speeding up the minimization process.

The solution to Eq. (1) is found by setting its gradient equal to zero, i.e.,

$$\nabla_{\delta \mathbf{v}} J = (\delta \mathbf{v}^k - \mathbf{d}^{b,k-1}) + \mathbf{U}^\top \mathbf{G}^{k-1 \top} \mathbf{R}^{-1} (\mathbf{G}^{k-1} \mathbf{U} \delta \mathbf{v}^k - \mathbf{d}^{o,k-1}) = \mathbf{0}. \quad (9)$$

This yields the solution to the k th linearization:

$$\delta \mathbf{v}^k = (\mathbf{I}_n + \mathbf{U}^\top \mathbf{G}^{k-1 \top} \mathbf{R}^{-1} \mathbf{G}^{k-1} \mathbf{U})^{-1} (\mathbf{d}^{b,k-1} + \mathbf{U}^\top \mathbf{G}^{k-1 \top} \mathbf{R}^{-1} \mathbf{d}^{o,k-1}) = - [\mathcal{H}_{\delta \mathbf{v}}]^{-1} \nabla_{\delta \mathbf{v}} J|_{\delta \mathbf{v}^k = \mathbf{0}}, \quad (10)$$

where $\mathcal{H}_{\delta \mathbf{v}} = \nabla_{\delta \mathbf{v}}^2 J$ is the Hessian of Eq. (7). In addition to their large size, \mathbf{G} and \mathbf{G}^\top are not often known explicitly and can only be multiplied by vectors through the integration of a TLM or ADM, respectively. As a result, $\mathcal{H}_{\delta \mathbf{v}}$ and its inverse are too large to store and calculate explicitly. The inverse Hessian is generally approximated through an iterative minimization (e.g., conjugate gradient), called the inner loop, while the successive relinearizations are performed across outer loop iterations. Finite precision and the problem dimension, n , prevent Eq. (9) from being exactly equal to zero. Increasing the number of inner loop iterations to approach such an objective does not necessarily speed up convergence for the full nonlinear problem. Large innovations, $\mathbf{d}^{o,k}$, may remain after relinearization around the new state, $\mathbf{x}^k = \mathbf{x}^{k-1} + \mathbf{U} \delta \mathbf{v}^k$. The balance between computational expense and accuracy is chosen for each application.

2.3.2 Log-normal control variables

The positive definite nature of atmospheric chemical emissions combined with uncertainties that are potentially greater

than 100 % sets them apart from most CVs sought in meteorological data assimilation. The cost function in Eq. (1) is derived assuming unbiased Gaussian statistics in both the background errors and model–observation errors. Emissions are more likely to be log-normally distributed, since individual sources are found from the products of variables which themselves are also positive definite. In order to ensure positive definiteness, the ratios of modeled (posterior, E_a) to tabulated inventory (prior, E_b) emissions in all grid cells are gathered into a vector, $\boldsymbol{\beta} = e^{\mathbf{x}_a}$, such that

$$E_{a,j} = E_{b,j} \beta_j, \quad (11)$$

for CV member j . Each β_j is a “linear scaling factor”, while “exponential scaling factors” comprise the posterior CV vector, \mathbf{x}_a . In this framework, \mathbf{x}_b is the background exponential scaling factor. Setting $\mathbf{x}_b = \mathbf{0}$ is equivalent to assuming that the inventory emissions are the prior. Equation (11) is expressed within the G operator and its Jacobian. \mathbf{x} is resolved on the grid scale and across hourly discretized emission rates; the temporal resolution is customizable for particular applications.

Although other emission scaling forms have proven effective (Bergamaschi et al., 2009; Jiang et al., 2015), we stick with exponential scaling factors here both as a first demonstration and to be consistent with log-normal statistics for emission rates. Fletcher and Zupanski (2007) showed that a cost function utilizing this exponential transform – which was previously applied to emission inversions by, e.g., Müller and Stavrou (2005), Elbern et al. (2007), and Henze et al. (2009) – converges toward the median of a multivariate log-normal distribution for $\boldsymbol{\beta}$. Our approach enables the use of existing WRFDA optimization algorithms, with a simple modification described in Sect. 2.3.5.

Model–observation concentration errors might also be treated as being log-normally distributed, since concentrations are positive definite. Still, the positive definite constraint on emissions ensures that the same applies to modeled concentrations, and we find that treatment to be effective. Introducing log-normality in the observations would corrupt the quadratic form of Eq. (1), which is necessary to derive the closed form solution of the additive increment in Eq. (10). Two alternatives to our approach that include log-normal observations are proposed by Fletcher and Jones (2014), who introduced a geometric incremental formulation with a non-quadratic cost function, and Song et al. (2016), who devised a quadratic approximation to the additive incremental log-normal cost function.

The scaling factor control variables necessitate a special treatment of prior error variance. The common practitioner may have some intuition about multiplicative emission uncertainties in $\boldsymbol{\beta}$ space (e.g., “factor of 2, 3, 4, etc.”), but not of the variance in exponential CV (\mathbf{x}) space that would populate the diagonal terms of \mathbf{B} . A vector that follows a multivariate log-normal distribution ($\boldsymbol{\beta} \sim \mathcal{LN}(\boldsymbol{\mu}, \mathbf{B})$) is simply

the exponential of a different vector that follows a multivariate Gaussian distribution (i.e., $\mathbf{x} \sim \mathcal{N}(\boldsymbol{\mu}, \mathbf{B})$). According to, e.g., Halliwell (2015), the sample mean and covariance of $\boldsymbol{\beta}$ across many realizations are

$$\mathbb{E}[\boldsymbol{\beta}^0]_i = \boldsymbol{\mu}_{\beta^0} = \exp\left(x_{b,i} + \frac{1}{2}\mathbf{B}_{x,ii}\right) \quad (12)$$

and

$$\mathbf{B}_{\beta^0,ij} = \exp\left[x_{b,i} + x_{b,j} + \frac{1}{2}(\mathbf{B}_{x,ii} + \mathbf{B}_{x,jj})\right](\exp\mathbf{B}_{x,ij} - 1), \quad (13)$$

respectively, where i and j are general indices coinciding with individual CV members, \mathbb{E} is the expectation operator and \exp is the natural exponential function. The subscript β^0 indicates a variable is evaluated in log-normal space in the zeroth outer iteration, when $k = 0$, and the subscript x indicates an evaluation in Gaussian CV space. In that Gaussian space, \mathbf{x}_b is the mean, median, and mode. As Eq. (12) shows, the expected value, or mean, of $\boldsymbol{\beta}^0$ is not equal to its median, $\exp x_{b,i}$, the latter being the central tendency we find by minimizing Eq. (7).

Equation (13) has not been used in previous emission inversions to translate relative emission uncertainties into the exponential space. When grid-scale relative emission uncertainties are less than $\times 3$, there is not much error in assuming that

$$(\sigma_{\beta^0,i} + 1)^2 \approx \frac{\exp(x_{b,i} + \sigma_{x_b,i})}{\exp(x_{b,i} - \sigma_{x_b,i})} = (\exp\sigma_{x_b,i})^2,$$

which is equivalent to

$$\sigma_{\beta^0,i} + 1 \approx \exp\sigma_{x_b,i} \quad (14)$$

and its inverse

$$\sigma_{x_b,i} \approx \log(\sigma_{\beta^0,i} + 1). \quad (15)$$

$(\sigma_{\beta^0} + 1)$ is the multiplicative uncertainty. For example, $\sigma_{\beta^0} = 2$ gives a factor of 3 ($\times 3$) relative emission uncertainty. For our case, where $\mathbf{x}_b = \mathbf{0}$, Eq. (14) diverges from Eq. (13) by less than 3 % in terms of an error in $(\sigma_{\beta^0,i} + 1)$ for $\sigma_{x_b} \in [0, \log(2)]$, but reaches 100 % mismatch at $\sigma_{x_b} = \log(4.2)$. The procedure we describe below should be followed when grid-scale uncertainties are probably above $\times 2$, such as for high-resolution inversions of BB sources. Simplifying Eq. (13) for a diagonal term, the i th prior variance of β^0 is

$$\sigma_{\beta^0,i}^2 = \exp\left[2x_{b,i} + (\sigma_{x_b,i})^2\right]\left[\exp(\sigma_{x_b,i})^2 - 1\right]. \quad (16)$$

This is identical to the variance transformation between univariate log-normal and Gaussian distributions. However, we want the inverse of this relationship,

$$\sigma_{x_b,i} = \sqrt{\log\left[1 + \frac{(\sigma_{\beta^0,i})^2}{\exp(2x_{b,i} + (\sigma_{x_b,i})^2)}\right]}. \quad (17)$$

With an initial guess of $\sigma_{x_b,i} = 0$, Eq. (17) converges in recursion for reasonable ranges of $\sigma_{\beta^0,i}$. This transformation only needs to be applied during preprocessing, and only once for each unique value of prior relative emission uncertainty.

2.3.3 Gaussian covariance

The error covariance matrices in Eq. (7) are estimated using existing knowledge of the underlying system. We assume that the off-diagonal covariances in \mathbf{B} are Gaussian in nature. These are defined through the CVT in WRFDA-Chem, which only differs from that of WRFDA in order to account for the temporal distribution of emissions. The transform $\delta\mathbf{x}^k = \mathbf{U}\delta\mathbf{v}^k$ is performed through two separate operations as $\mathbf{U} = \mathbf{U}_t\mathbf{U}_h$. Although the horizontal transform (\mathbf{U}_h) only deals with correlations in the x and y directions, and the temporal transform (\mathbf{U}_t) only does so in the temporal dimension, they are both $n \times n$, with sub-matrices along the diagonal of dimension $(n_x n_y) \times (n_x n_y)$ and $(n_t) \times (n_t)$, respectively. The computational overhead of multiplying by either transform is reduced by only handling the non-zero elements. \mathbf{U}_h is carried out using recursive filters and the scalar correlation length scale, L_h (Barker et al., 2004).

The temporal transform, \mathbf{U}_t , is constructed in a similar fashion to the vertical transform in WRFDA for meteorological CVs (Barker et al., 2004), except that herein we use all of its eigenmodes. The user specifies the duration of emission scaling factor bins (in minutes), the temporal correlation timescale (L_t , in hours), and the grid-scale relative emission uncertainty, σ_x . WRFDA-Chem converts these selections to a covariance sub-matrix $\mathbf{B}_t = \boldsymbol{\Sigma}\mathbf{C}\boldsymbol{\Sigma} \in \mathbb{R}^{n_t \times n_t}$, where \mathbf{C} is the temporal correlation matrix and $\boldsymbol{\Sigma} = \sigma_x \mathbf{I}_{n_t}$. \mathbf{B}_t is square, symmetric, and positive-definite. Similar to Saide et al. (2015), \mathbf{C} is defined using an exponential decay,

$$C_{ij} = e^{-\frac{\Delta t}{L_t}}, \quad (18)$$

where Δt is the time elapsed between the beginning of two particular emission steps. The covariance is decomposed into eigenmodes as $\mathbf{B}_t = \mathbf{E}_t \boldsymbol{\Lambda}_t \mathbf{E}_t^T$; these are readily calculated, because the dimension of \mathbf{B}_t is the square of the number of emission time steps (e.g., 24 steps for hourly scaling factors in a single-day inversion). Throughout the optimization, the temporal transform is carried out through multiplication by

$$\mathbf{U}_t = \begin{bmatrix} \mathbf{E}_t \boldsymbol{\Lambda}_t^{1/2} & \dots & \mathbf{0} \\ \vdots & \ddots & \vdots \\ \mathbf{0} & \dots & \mathbf{E}_t \boldsymbol{\Lambda}_t^{1/2} \end{bmatrix} \quad (19)$$

and its transpose.

The model–observation errors are also assumed to be Gaussian, and their covariance matrix, \mathbf{R} , is assumed diagonal. For each measurement, p , the total variance is defined as the sum of observation ($\sigma_{p,o}^2$) and model ($\sigma_{p,m}^2$) components, following the approach by Guerrette and Henze

(2015). $\sigma_{p,m}$ is determined from an ensemble of 156 WRF-Chem model configurations. Each member uses a unique combination of options for PBL mixing, surface layer, LSM, and longwave and shortwave radiation, and includes or excludes microphysics and subgrid cumulus convection. $\sigma_{p,o}$ accounts for instrument precision, representativeness error, and averaging of measurements to the model resolution. We do not use the weighting term previously defined by Guerrette and Henze (2015), because small residuals with low uncertainty do not appear to hinder the inversion process. Refer to that work for more particular details of how $\sigma_{p,m}^2$ and $\sigma_{p,o}^2$ are calculated.

2.3.4 Posterior error

Posterior uncertainty is a useful measure to diagnose the value of an emission inversion. While areas where uncertainty has been reduced from the prior include new information from the observations, areas without uncertainty reduction are simply a new realization of the prior. In a region of linear behavior of a nonlinear DA cost function, and when $\delta\mathbf{x}$ is normally distributed, the posterior covariance, \mathbf{P}^a , is equal to the inverse Hessian of Eq. (1) (e.g., Thacker, 1989; Fisher and Courtier, 1995):

$$\mathbf{P}^a = [\mathcal{H}_{\delta\mathbf{x}}]^{-1}, \quad (20)$$

where

$$\mathcal{H}_{\delta\mathbf{x}} = \mathbf{B}^{-1} + \mathbf{G}^{k-1\top} \mathbf{R}^{-1} \mathbf{G}^{k-1}. \quad (21)$$

Combining this with the expression for the Hessian of Eq. (7) we used in Eq. (10) gives a conversion from the transformed variable space

$$\mathcal{H}_{\delta\mathbf{v}} = \mathbf{U}^\top \mathcal{H}_{\delta\mathbf{x}} \mathbf{U}. \quad (22)$$

Using a Lanczos recurrence to solve the inner loop optimization problem in Eq. (7) has the benefit of producing the means to approximate $[\mathcal{H}_{\delta\mathbf{v}}]^{-1}$, which we demonstrate in Appendix B. The final result of that derivation is the posterior error,

$$\begin{aligned} \mathbf{P}^a &= \mathbf{U} [\mathcal{H}_{\delta\mathbf{v}}]^{-1} \mathbf{U}^\top \\ &\approx \mathbf{B} + \sum_{k_i=1}^l \left(\lambda_{k_i}^{-1} - 1 \right) (\mathbf{U} \hat{\mathbf{v}}_{k_i}) (\mathbf{U} \hat{\mathbf{v}}_{k_i})^\top, \end{aligned} \quad (23)$$

in terms of the eigenvectors of $\mathcal{H}_{\delta\mathbf{v}}$, $\hat{\mathbf{v}}_{k_i} = \mathbf{Q}_l \hat{\mathbf{w}}_{lk_i}$. Each inner iteration, k_i , leading up to the current iteration l of the Lanczos optimization, produces (1) a new Lanczos vector in the orthonormal matrix $\mathbf{Q}_l = [\hat{\mathbf{q}}_1, \dots, \hat{\mathbf{q}}_l]$ and (2) a new row and column in a tridiagonal matrix \mathbf{T}_l , whose k_i th eigenpair is $(\lambda_{k_i}; \hat{\mathbf{w}}_{lk_i})$. \mathbf{P}^a is a low-rank update to \mathbf{B} , because $l \ll n$ due to the wall-clock requirements of running the TLM and ADM once per iteration. Equation (23) is consistent with earlier publications (Fisher and Courtier, 1995; Meirink et al., 2008).

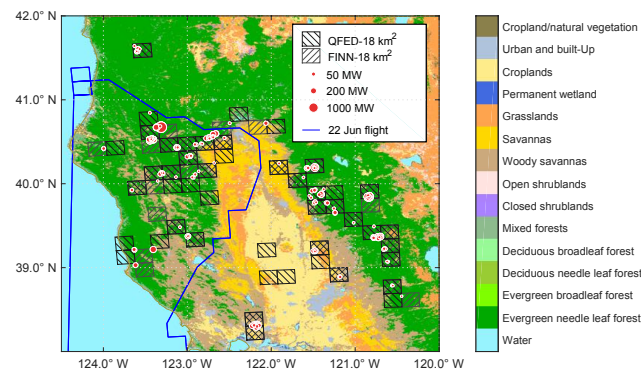


Figure 2. Land category types, MODIS fire hotspot detections on 21 and 22 June 2008, sized by FRP, and 18 km \times 18 km gridded FINNv1.0 and QFED emission locations.

2.3.5 Nonlinear optimization

For each outer loop iteration, $\delta\mathbf{x}^k$ must be small enough to keep the error associated with the TL assumption, Eq. (5), below some threshold. Otherwise the cost function may actually increase between successive k 's. However, the nonlinearity of the log-normal prior emission errors contributes to failures in that respect. Violation of the TL assumption and potential solutions are discussed in several DA works. The prevailing strategy in chemical 4D-Var is to apply a quasi-Newton optimization (e.g., Henze et al., 2009; Bergamaschi et al., 2009), eliminating the inner-outer loop structure of GN. Implementing this approach in WRFDA with posterior error estimation would be a considerable additional effort. Also, as we mentioned in Sect. 2.1, using the tangent linear model in the inner loop presents computational advantages for dual resolution 4D-Var.

There are several alternative approaches, which stem from the equivalence between incremental 4D-Var and GN. Gratton et al. (2013) discuss application of GN in a trust region framework, which has the limitation that a portion of the computationally expensive outer loop increments will be rejected. Some authors have successfully applied the Levenberg–Marquardt algorithm in EnKF (e.g., Chen and Oliver, 2013; Mandel et al., 2016) by adding a regularization term to the cost function. That method requires one to perform the inner loop approximation of $[\mathcal{H}_{\delta\mathbf{v}}]^{-1}$ multiple times, once for each value of a scalar regularization parameter. A similar and cheaper approach is damped GN (DGN), which changes the inner loop increment in Eq. (10) to

$$\delta\mathbf{v}^k = -\eta^k [\mathcal{H}_{\delta\mathbf{v}}]^{-1} \nabla_{\delta\mathbf{v}} J|_{\delta\mathbf{v}^k=0}, \quad (24)$$

and uses a line search to find an optimal scalar $\eta^k \in (0, 1]$ after the completion of each outer loop iteration (Kelley, 1999). DGN is based on the Armijo rule, which states that the increment found by GN points toward a direction of lower J ; if the step size terminus is outside the linear behavior of the model, decrease the step size. This strategy is implemented

in WRFDA-Chem for log-normally distributed emission errors.

3 ARCTAS-CARB case study

3.1 Inversion setup

From late May until 20 June 2008, the southwestern US experienced a very dry period with little to no cloud cover appearing in MODIS true color imagery, and no recorded rainfall for most of California. On 21 June, the Aqua and Terra satellites recorded cloud cover for much of northern California, south of San Francisco, and along the Sierra Nevada mountain range, and there were widespread lightning strikes overnight. As is shown in Fig. 1, there was a spike in fire detections during the night between 21 and 22 June. Thus, from the morning through evening of 22 June, California experienced a transient fire initiation event. The wildfires burned well into July, exacerbating poor air quality throughout the state. The 20 June flight of ARCTAS-CARB characterized northern California anthropogenic sources, but was not influenced by fires. The 22 June flight embarked from Los Angeles, transited the offshore Pacific inflow, flew directly through smoke from forest fires in northern California, and then returned down the coastline. That flight encountered anthropogenic sources of BC in the morning, and BB sources for the remainder after returning to land. The 24 June flight passed back and forth in the downwind region between Los Angeles and San Diego, measuring the outflow from those cities and the transportation between them, and 1-day old diluted BB outflow from the north. A fourth flight on 26 June flew in the free troposphere from Los Angeles, north over the fires, and exited the model domain to the east.

We use WRFDA-Chem 4D-Var to constrain BB and anthropogenic aerosols on 3 days during ARCTAS-CARB using aircraft and IMPROVE surface observations. We utilize aircraft measurements of absorbing carbonaceous aerosol at 10 s intervals from the single-particle soot photometer (SP2) on 22, 24, and 26 June (Sahu et al., 2012). For this study, we assume equivalency between the SP2 measurement and modeled BC, and re-average to the 90 s model time step using the revision 3 product, a process described in Guerrette and Henze (2015). We also use 24 h average surface observations of light absorbing carbon (LAC) on 23 and 26 June (Malm et al., 1994), assuming an equivalence with modeled BC, and ignoring the 7 % high bias relative to the SP2 found by Yelverton et al. (2014). All treatments of observations are identical to those described in Guerrette and Henze (2015), including an analysis of model–observation BC mismatch that feeds into the inverse modeling study.

Using measurements from 22, 23, and 24 June, the 4D-Var system constrains anthropogenic and BB sources simultaneously. Data collected between 07:00:00 and 16:00:00 LT on 22 June are used in an inversion from 22 June, 00:00:00 UTC

Table 1. Emission inversion scenarios.

	Scenario	BB inventory	L_h	Obs. used (day)
22 Jun	FINN_STD	FINNv1.0	36 km	ARCTAS-CARB (22)
	FINN_L18	FINNv1.0	18 km	ARCTAS-CARB (22)
	QFED_STD	QFEDv2.4r8	36 km	ARCTAS-CARB (22)
	QFED_L18	QFEDv2.4r8	18 km	ARCTAS-CARB (22)
	FINN_V1.5	FINNv1.5	36 km	ARCTAS-CARB (22)
23/24 Jun	FINN_STD	FINNv1.0	36 km	IMPROVE (23) ARCTAS-CARB (24)
	QFED_STD	QFEDv2.4r8	36 km	IMPROVE (23) ARCTAS-CARB (24)
	ACFT	FINNv1.0	36 km	ARCTAS-CARB (24)
	SURF	FINNv1.0	36 km	IMPROVE (23)

to 23 June, 00:00:00 UTC, during which time WRF-Chem is run freely, without nudging. The emission scaling factors for this 24 h time period for both source types are applied to subsequent days from 23 to 26 June in a cross-validation experiment. The 24 and 26 June aircraft and 23 and 26 June surface observations are used to analyze the utility of observationally constrained scaling factors found on 1 day to fix source errors on subsequent days. The 23 and 24 June surface and aircraft data are used in a 48 h inversion from 23 June, 00:00:00 UTC to 25 June, 00:00:00 UTC, also without nudging. Cross-validation is performed for these source estimates using 26 June surface and aircraft data.

Through preliminary testing, we found that horizontal correlation length scales on the order of the grid spacing provide the lowest posterior cost function. For both time periods, this length scale is set to twice the grid scale, $L_h = 36$ km. The emission scaling factors are aggregated in each hour, which coincides with the emission file reading interval for both source types. The correlation scale is set to $L_t = 4$ h, following Saide et al. (2015). In addition to spreading error information across adjacent grid cells, the correlation scales reduce the effective number of CVs. Through sensitivity tests where we considered the smoothness of the posterior and the stationary posterior cost function value, and after consulting published values for regional emission uncertainties (see Sect. 1) in different global settings, we use a relative grid-scale BB uncertainty of $\times 3.8$. The BB uncertainty might also be approximated from the ratio of prior domain-wide total emissions between FINNv1.0 and QFED, which is given in Table 5 as $\times 3.5$. If the median emission strength lies in the middle of QFED and FINNv1.0, then the prior domain-wide relative uncertainty is $\times \sqrt{3.5} = \times 1.8$. The uncertainty would then need to be inflated further to account for spatial and temporal disaggregation and the possibility that grid-scale sources from the two inventories do not bound the true value (see Sect. 3.3). The prior anthropogenic grid-scale relative uncertainty is set to $\times 2$, which is within the reasonable bounds discussed in Sect. 1.

In addition to these standard settings, several sensitivity scenarios are used to gauge the sensitivity of the posteriors during two time periods to alternative inversion settings. The full set of scenarios are summarized in Table 1, and are as follows. FINNv1.0 is used as the default BB inventory in a scenario called FINN_STD for both inversion periods. QFED_STD uses the QFEDv2.4r8 BB inventory. Both FINN_L18 and QFED_L18 use $L_h = 18$ km. FINN_V1.5 utilizes the FINNv1.5 BB inventory. For the 23/24 June inversion, we show results for both QFED_STD and FINN_STD, the latter of which includes variations where either surface or aircraft observations are excluded. The number of aircraft observations is $N_{\text{obs}} = 241$ on 22 June and $N_{\text{obs}} = 302$ on 24 June. There were $N_{\text{obs}} = 35$ active surface sites on 23 June, 13 of them within California. We use six outer iterations consisting of 10 inner iterations each. Given the number of inner iterations used, and the wall-time of the tangent linear plus the adjoint ($\times 10$ longer than the nonlinear model), the cost of 4D-Var is approximately $\times 600$ more than that of a single forward simulation, which is much cheaper than using finite difference methods to approximate derivatives instead of the linearized models when $n \sim 10^5$.

3.2 Posterior model performance

For a linear model operator and Gaussian distributed errors, the cost function can be used to evaluate the consistency of the statistics in **B** and **R**. The χ^2 criteria states that the posterior cost function should be equal to $\frac{1}{2}N_{\text{OBS}}$ (e.g., Tarantola, 2005). The convergence properties of the 22 and 23/24 June inversion scenarios are shown in the outer loop cost function progression in Fig. 3. All of the 22 June scenarios led to comparable cost function values at numerical convergence, as shown in Fig. 3. The gradient norms are also reduced by nearly two orders of magnitude in all cases. In all of the scenarios, J converges to approximately N_{OBS} , indicating that a portion of the model errors are not fully spanned by prior emission errors. For the 23/24 June inversion, QFED_STD reaches a lower cost function value, and both scenarios achieve similar χ^2 values as the 22 June cases. Scrutinizing other sources of error (e.g., initial and boundary conditions for BC and meteorological variables, transport, BB plume rise, and model discretization) either independent from source strengths or simultaneously in the inversion framework should elicit further cost function reductions. Considering the top subplot in Fig. 4, the non-emission sources of error on 22 June are evident when the prior and posterior predictions are on top of each other, and remain on the edges of the low probability uncertainty region. For example, the observations before 08:00 LT after takeoff from Edwards are likely sensitive to the Pacific inflow, but not early morning emissions. Since these locations have relatively small uncertainties, the posterior cost function will never be reduced there.

Figure 4 also shows that during the inversion period the posterior is within the combined model–observation uncertainty (see Sect. 2.3.3) much more often than the prior. In the afternoon, when the DC-8 passed over the wildfires, an increase in posterior emissions captures several of the observed BC peaks. The posterior is able to match the high-resolution variability of the observations at 13:30 LT, which may support the validity of the temporal averaging scheme. The only time during the inversion when the forecast degrades is for an observed peak at 22 June, 08:00 LT. The larger absolute observation uncertainty at that time relative to that at 08:30 LT enforces a weaker constraint in the inversion. Coupled with the assumed relative emission error correlation length scale and the close proximity of these two measurements, that stronger constraint at 08:30 LT dominates the morning anthropogenic emission analysis increment.

The R^2 coefficients and slopes for linear fits between the prior and posterior and both aircraft and surface observations are summarized in Tables 2 and 3. Those results include cross-validation data on non-inversion days, which is discussed in Sect. 3.5. For both inversion periods, there are considerable model performance improvements for observations that are used in the inversion. FINN_STD improves R^2 from 0.11 to 0.82 and slope from 0.26 to 0.8 on 22 June. QFED_STD improves R^2 from 0.03 to 0.73 and slope from 0.34 to 0.71. Similar improvements occur for 23 June surface observations during the 23/24 June inversion. The posterior match to 24 June aircraft observations is improved, but not nearly as much as the other two data sets. The 22 June inversion results are also shown in Fig. 5, where the progression of the fit parameters is shown for the multiple scenarios. While all scenarios show similar improvements, the FINN_STD and QFED_STD results indicate the posteriors are still underpredicting many low and high concentrations. A similar phenomenon occurs for the 24 June observations in Fig. 6 in the inversion that uses both surface and aircraft observations. On both 22 and 24 June, the remaining low bias is either due to large prior observation and model error (diagonal of **R**) or due to the prior errors not being sensitive to emission increments.

For the appreciable measured BC concentrations ($> 0.25 \mu\text{g m}^{-3}$), which are likely caused by a source within the model domain and simulation period, the lack of a source–receptor relationship is likely caused by low resolution. Changing a point source to a grid-scale area source changes its effective location. Temporal averaging of the observations will not necessarily solve that problem since perfectly modeled transport could still send a mislocated source in an entirely different direction than the truthfully located source. This effect is evident for valley fires (Strand et al., 2012), since placing the sources in the basin or spreading them throughout the basin and the peaks will result in different “downwind” concentrations. Downwind might be a very different direction if the convective-scale winds contribute more information than the mesoscale winds

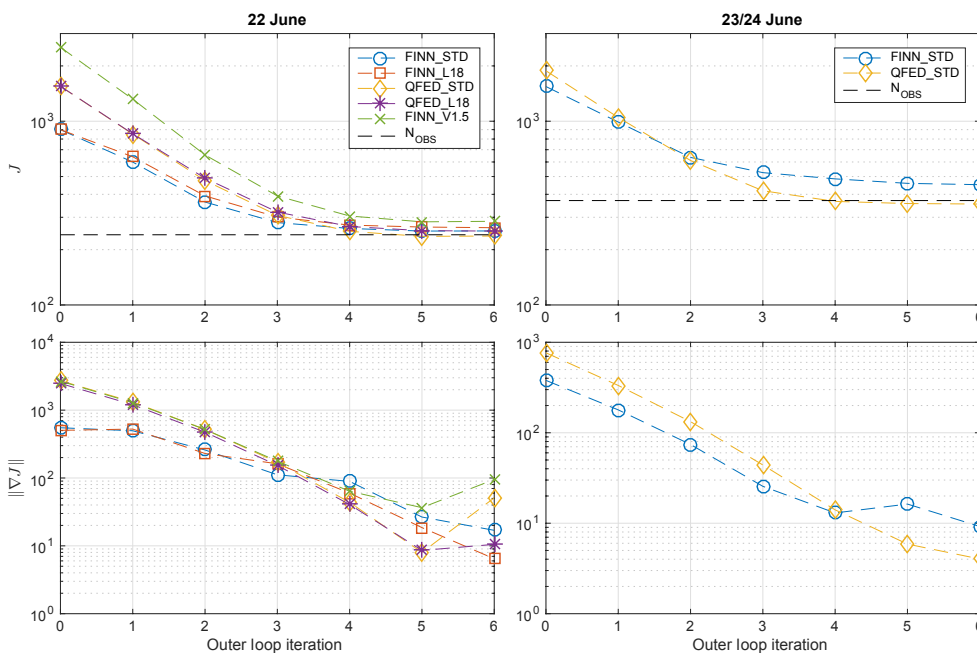


Figure 3. Outer loop cost function and gradient norm evaluations for the 22 June (left column) and 23/24 June (right column) inversions.

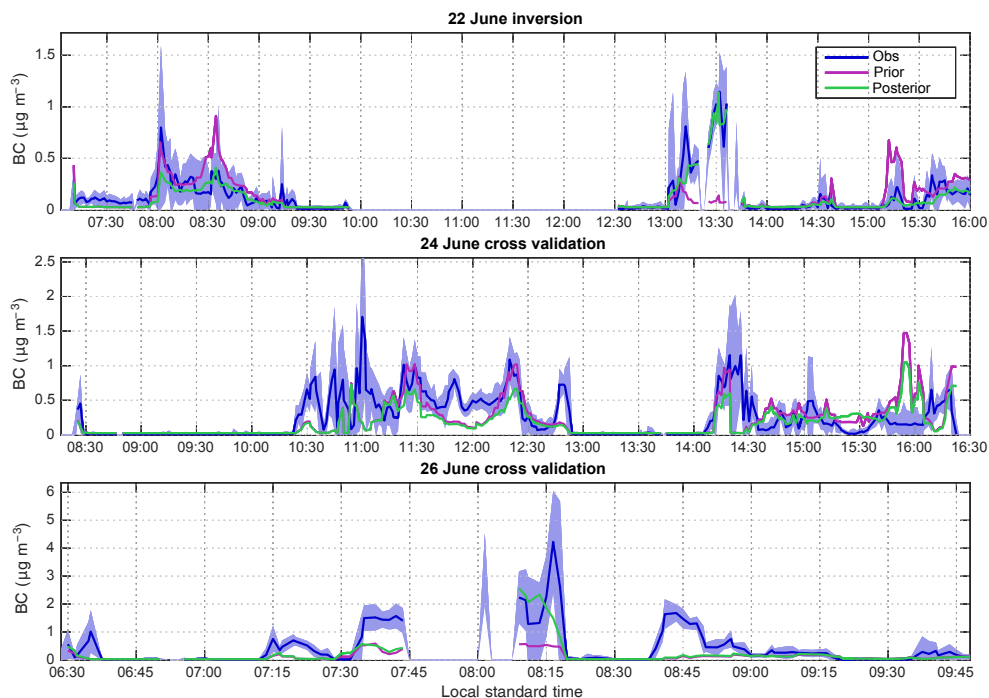


Figure 4. Temporal variation of observed, prior, and posterior BC concentrations during ARCTAS-CARB. The model values are obtained with the FINN_STD inversion scenario. The shaded area encompasses 2 standard deviations around the observations, which includes both model and observation uncertainty.

to the true source–receptor relationship. Since the emissions are smoothed in the model and not in reality, the mislocation is more likely to cause underprediction than overprediction.

3.3 Posterior emissions

Figure 7 shows the prior and posterior BB emissions for FINN_STD and QFED_STD during both simulation periods.

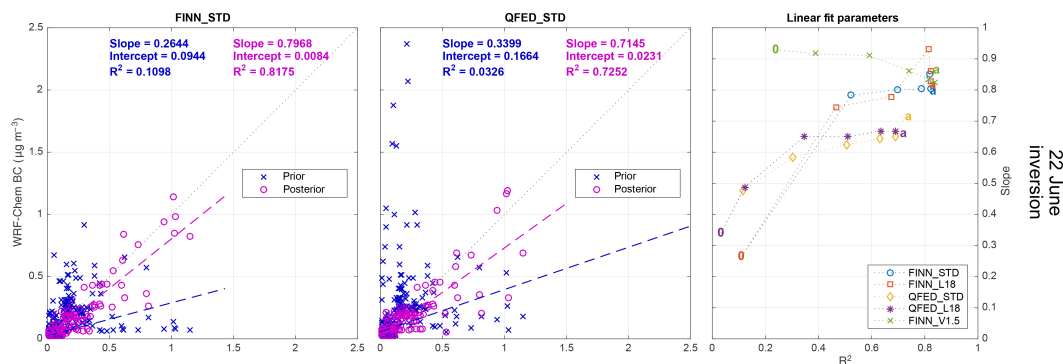


Figure 5. Prior and posterior model versus 22 June ARCTAS-CARB observations for the 22 June inversion. The left two plots are for FINN_STD and QFED_STD. The plot on the right shows the progression of the slope and R^2 from the prior, “0”, to the posterior, “a”, for similar linear regressions in all scenarios.

Table 2. Aircraft observation linear regression characteristics for the prior (background, b) and posterior (analysis, a).

Obs. date →		22 Jun, $N_{\text{obs}} = 241$				24 Jun, $N_{\text{obs}} = 301$				26 Jun, $N_{\text{obs}} = 117$			
Inversion scenario		R^2		slope		R^2		slope		R^2		slope	
↓		b	a	b	a	b	a	b	a	b	a	b	a
22 Jun	FINN_STD	0.11	0.82	0.26	0.80	0.18	(0.15)	0.38	(0.25)	0.56	(0.52)	0.15	(0.49)
	QFED_STD	0.03	0.73	0.34	0.71	0.15	(0.23)	0.43	(0.37)	0.59	(0.53)	0.39	(0.43)
23/24 Jun	FINN_STD	–	–	–	–	0.17	0.52	0.35	0.56	0.59	(0.16)	0.15	(0.11)
	QFED_STD	–	–	–	–	0.11	0.52	0.36	0.55	0.63	(0.44)	0.41	(0.15)
	ACFT	–	–	–	–	0.17	0.53	0.35	0.57	0.59	(0.29)	0.15	(0.08)
	SURF	–	–	–	–	0.17	(0.17)	0.35	(0.40)	0.59	(0.13)	0.15	(0.17)

Distinct improvement (bold). Distinct degradation (italic). Cross-validation (parentheses).

In that figure there are several outlined emission areas (EAs); each EA was chosen to identify regions where a subset of the grid-scale analysis increment ($\delta x_{\text{EAX}} \subset \delta x$) from both prior inventories is of a similar sign. The coordinates of the EAs are listed in Table 4. The two inversions do not reach identical total posterior BC emissions, but they do converge in certain aspects. Table 5 gives the emission subtotals for the EAs. During both inversions, each EA has emission increments of the same sign for both scenarios. Therefore, while domain-wide sources seem to be bounded by the two priors (as evidenced by their convergence), the same might not be true within the individual EAs. EA3, which accounts for the smallest average posterior total, is the only region where the magnitude of the log ratio between QFED and FINN is smaller in the posterior on 22 June. The ratio is reduced in EA2, but there the FINN posterior is $\times 2$ larger than that for QFED. On 23/24 June, the two scenarios have less posterior spread in all of the EAs. Although Table 5 indicates large changes in source strengths across the EAs, Fig. 8 reveals that a majority of the absolute emission increment (posterior minus prior) in both FINN_STD and QFED_STD arose in only a few grid cells, often where the prior has the largest magnitude. The linear scaling factor pattern is similar be-

tween the two scenarios, with those for QFED_STD shifted toward decreases due to the high prior bias.

The temporal distributions of prior and posterior BB emissions within the four EAs are shown in Fig. 9 across all inversion scenarios on 22 June. The FINNv1.5 prior is an extreme outlier on the local afternoon of 21 June for EA1, EA2, and EA4. The same is true all day on 22 June for EA2, where the posteriors from other scenarios adjust toward the FINNv1.5 prior. Meanwhile, at other times when FINNv1.5 appears to converge toward the posteriors found using the other two priors, the prior relative uncertainty of $\times 3.8$ is too restrictive to allow full convergence, since the priors differ by $\times 10$. EA1 is characterized by decreases for all scenarios at all times. EA2, EA3, and EA4 exhibit early morning peaks between 03:00 and 06:00 LT that were not captured in the prior. In separate sensitivity tests, these peaks only appear when $L_t > 1$ h, and become more prevalent as L_t is increased. Saide et al. (2015) attributed similar behavior in posterior estimates of the 2013 Rim Fire to persistent large-scale burning. Zhang et al. (2012) found similar, less pronounced bimodal behavior for all of North America, which could be more noticeable in a regional inversion. Another possibility on 22 June 2008 is that the early morning burning is caused

Table 3. Surface observation linear regression characteristics for the prior (background, b) and posterior (analysis, a).

Obs. date →		23 Jun, $N_{\text{obs}} = 35$				26 Jun, $N_{\text{obs}} = 36$			
Inversion scenario		R^2		slope		R^2		slope	
↓		b	a	b	a	b	a	b	a
22 Jun	FINN_STD	0.06	(0.04)	0.26	(0.21)	0.03	(0.05)	0.10	(0.13)
	QFED_STD	0.16	(0.14)	0.44	(0.41)	0.10	(0.11)	0.20	(0.21)
23/24 Jun	FINN_STD	0.04	0.75	0.25	1.04	0.03	(0.28)	0.10	(0.28)
	QFED_STD	0.09	0.74	0.39	1.01	0.09	(0.15)	0.20	(0.16)
	ACFT	0.04	(0.05)	0.25	(0.27)	0.03	(0.03)	0.10	(0.09)
	SURF	0.04	0.74	0.25	1.02	0.03	(0.35)	0.10	(0.35)

Distinct improvement (bold). Distinct degradation (italic). Cross-validation (parentheses).

Table 4. Emission area coordinates. EA1–4 are used for BB totals and EA5–9 are used for anthropogenic totals.

	LON _{min}	LON _{max}	LAT _{min}	LAT _{max}
EA1	122.5° W	120.5° W	35.7° N	38.5° N
EA2	123.8° W	122.1° W	38.9° N	40.4° N
EA3	124.3° W	122.9° W	40.4° N	41.7° N
EA4	122.1° W	120.0° W	38.5° N	40.4° N
EA5	117.8° W	116.9° W	32.1° N	33.4° N
EA6	121.0° W	117.8° W	33.4° N	34.6° N
EA7	123.0° W	121.0° W	36.6° N	38.8° N
EA8	120.6° W	118.6° W	35.2° N	37.0° N
EA9	118.0° W	116.5° W	34.0° N	36.0° N
EA10	116.9° W	115.0° W	32.1° N	33.4° N

by the transient fire initiation event, which would explain the ramping of emissions for the QFED and FINNv1.5 posteriors in EA2. For both QFED and FINNv1.0, reducing the correlation length to $L_h = 18$ km reduces the analysis increment in all EAs. This is especially apparent in EA4 for FINN_L18, where the increment is negligible.

The differing diurnal patterns in EA2 across scenarios could be attributed to variation in plume heights, QFED re-gridding errors, and the regularization term of the cost function. The observations most sensitive to EA2 sources were captured within or very near fire plumes. Plume heights are calculated hourly in an online 1-D vertical mixing scheme in WRF-Chem (Freitas et al., 2007, 2010; Grell et al., 2011), which depends strongly on burned areas. With FINN, the areas are provided for each fire independently, while for QFED the areas use a default value of 0.25 km^2 per fire. In both cases, the maximum area burned per grid cell per day is 2 km^2 . The re-gridding error discussed in Sect. 2.2 introduces fire locational errors, especially in EA2. A small error in vertical or horizontal mapping of a discrete point source on the model grid could hinder the optimization in distinguishing it from others. The uniform relative uncertainty in the prior inhibits consolidation of multiple posteriors when the prior

spread is heterogeneous and sometimes very large. Quantifying the heterogeneity of uncertainty could contribute to posterior agreement between inversions using different priors, as well as to reducing the cost function.

The spread of local emissions provides some sense of that heterogeneity. Each EA covers a region approximately the size of a grid box in a global simulation with a chemical transport model. Due to the nature of variance aggregation, uncertainty grows as the grid scale gets smaller. In individual EAs, the spread between FINNv1.0 and QFED priors is $\times 2$ – $\times 6$ for both hourly (Fig. 9) and daily (Table 5) strength on 22 June. If the median emission strength lies in the middle, then a proxy for prior EA relative uncertainty is $\times \sqrt{2} - \times \sqrt{6} = \times 1.4 - \times 2.4$. Since the two inventories use identical diurnal patterns, the hourly estimate is missing information about uncertainties in daily emission timing. Using the posterior spread in a similar way gives approximate EA uncertainties of $\times \sqrt{3} - \times \sqrt{10} = \times 1.7 - \times 3.2$ on hourly scales and $\times \sqrt{2} - \times \sqrt{7} = \times 1.4 - \times 2.6$ on daily scales. This posterior estimate accounts for contributions in the prior definitions, including re-gridding, plume rise, and diurnal patterns. These ranges provide much more detail estimates than simply taking the domain-wide ratio of total emissions for the campaign period. However, the spread is itself missing information about uncertainty that could be found through carrying out similar inversions across an ensemble of model configurations and meteorological initial and boundary conditions (e.g., Lauvaux et al., 2016), or by comparing many more inventory priors (e.g., F. Zhang et al., 2014) and posteriors. All this is to say that the BB inventories used in this study are not provided with analytical estimates of uncertainty, and a lack of information for deriving such values at hourly grid scales is a topic for future research.

Figure 10 shows the total prior and posterior anthropogenic emissions and Fig. 11 displays the analysis increment and linear scaling factor for FINN_STD on 22 June and separately on 23–24 June. The only difference in QFED_STD, not shown here, is that anthropogenic scaling factors are shifted in the negative direction in the posterior,

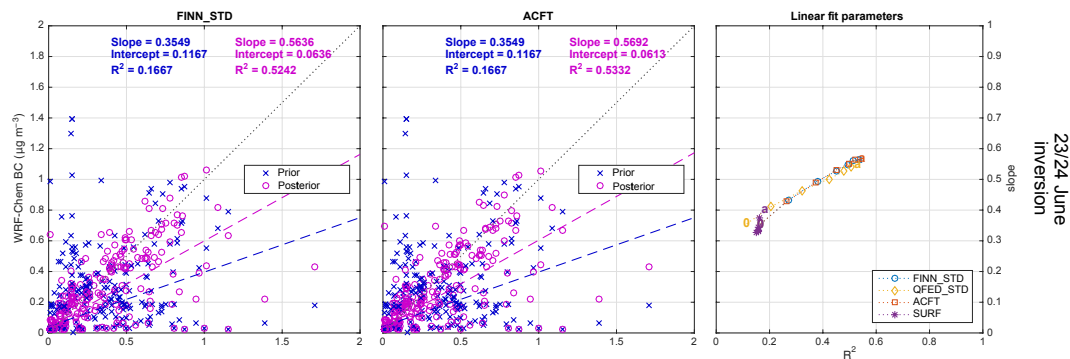


Figure 6. Prior and posterior model versus 24 June ARCTAS-CARB observations for the 23/24 June FINN_STD inversion. The left plot uses both IMPROVE (23 June) and ARCTAS-CARB observations in the inversion. The middle plot uses only ARCTAS-CARB. The plot on the right shows the progression of the slope and R^2 from the prior, “0”, to the posterior, “a”, for similar linear regressions.

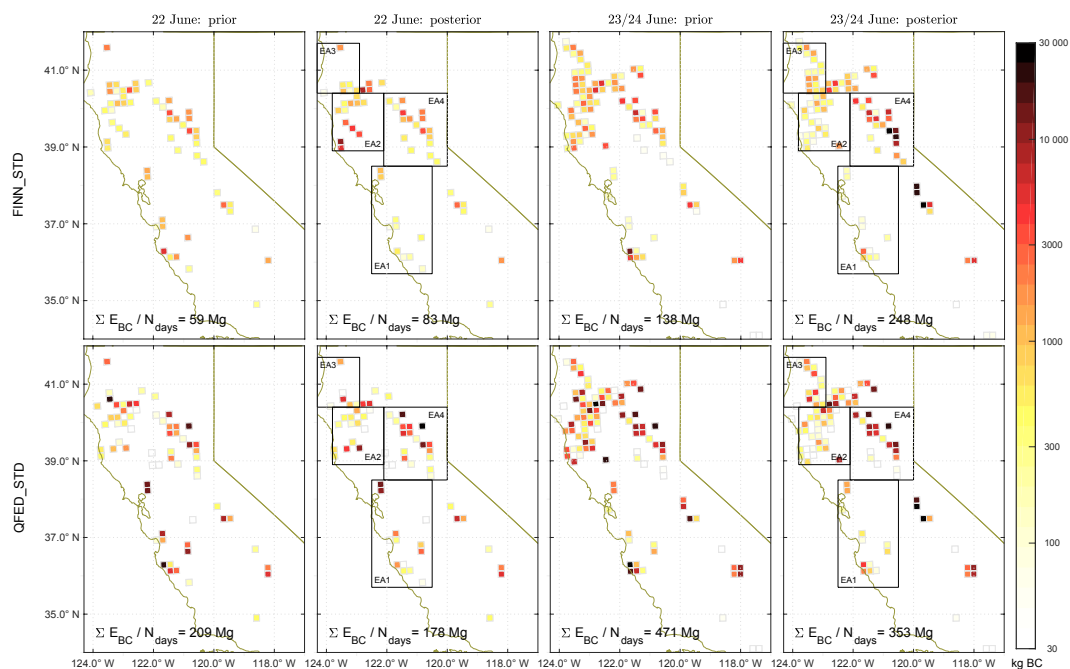


Figure 7. Prior and posterior grid-scale BB emissions of BC per 24 h for FINN_STD and QFED_STD on 22 June, 00:00–23:00 Z and 23 June 00:00–24 June 23:00 Z. All emissions are expressed for a 24 h average. EA1–4 are outlined with black boxes.

likely due to the higher bias in that BB prior. The increments found in a new set of EAs are presented in Table 6.

The 23 and 24 June observations provide much more detailed information about anthropogenic sources. The analysis increment reveals potentially misrepresented city-level emissions in the NEI05 prior. Posterior BC near Barstow, Victorville/Hesperia, Fresno, Edwards Air Force Base, and El Centro/Calexico are increased, while sources near the three coastal cities are decreased. Since Barstow is a crossroads for the BNSF and the Union Pacific railroads, and since Fresno, Victorville/Hesperia, and El Centro/Calexico lie at switching locations for major rail lines, the inversion results may suggest that the prior is missing diesel rail sources of BC.

However, for locations where the prior magnitude of BB and anthropogenic emissions are of similar magnitude, their posteriors are subject to projection from one sector to another. It is more likely that the low bias fire emissions north of Fresno are responsible for the prior underpredictions of 23 June surface concentration measurements exceeding $2 \mu\text{g m}^{-3}$ (see Fig. 5 of Guerrette and Henze, 2015). This is corroborated by the posterior BB emissions being scaled up near Fresno on 23 and 24 June, and by the much smaller model bias for IMPROVE on 22 June before the fires started.

There are also small negative increments near Los Angeles (EA6) and San Francisco (EA7) during both the 22 June and 23/24 June inversions, which are likely attributable to on-

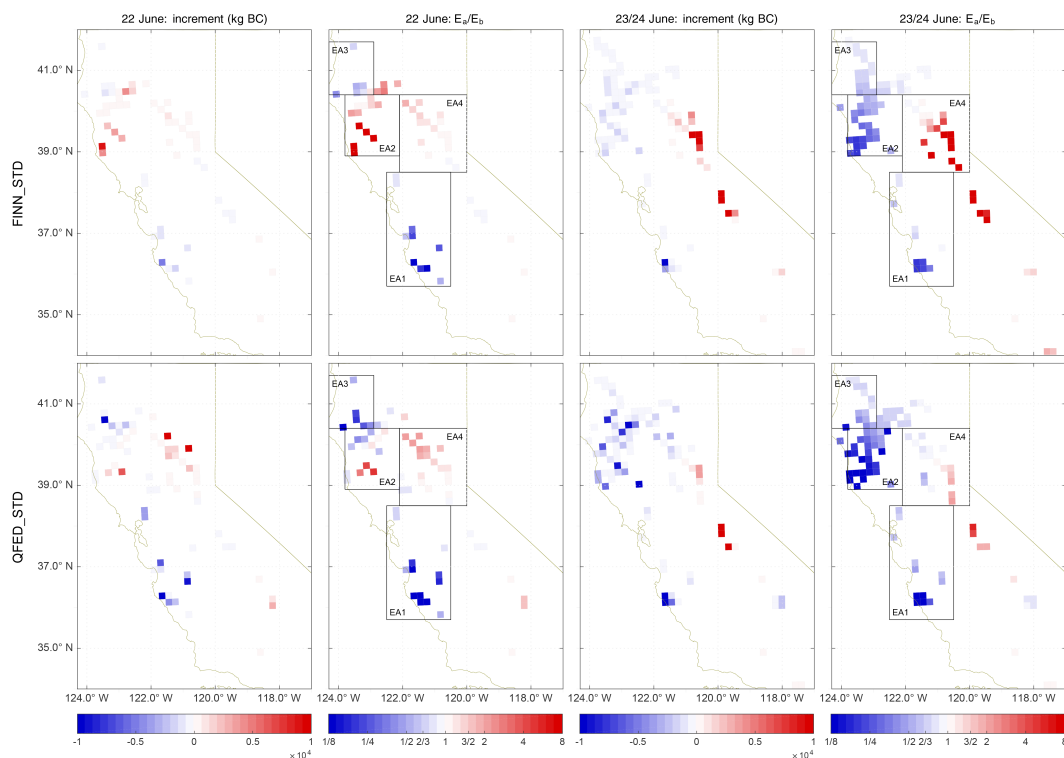


Figure 8. BB analysis increment (posterior minus prior) per 24 h and posterior linear scaling factor (β) for the two primary BB scenarios on 22 June 00:00–23:00 Z and 23 June 00:00 Z–24 June 23:00 Z. EA1–4 are outlined with black boxes.

road mobile sources. These results are consistent with model bias in surface and aircraft observations on 20 June near both of those cities (Guerrette and Henze, 2015). McDonald et al. (2015) found a decreasing trend in ambient measurements of BC and in a fuel-based bottom-up inventory for both Los Angeles and San Francisco from 1990 to 2010 that might not be captured for the 2008 model year by the snapshot in NEI05. Using a similar fuel-based approach, Kim et al. (2016) derived 2010 CO emissions in the South Coast Air Basin surrounding Los Angeles that are $\times 1/2$ the magnitude of NEI05. On-road and other mobile sources make up 36 and 62 % of that difference, respectively, and their bottom-up inventory matches more closely with NEI 2011. While not a perfect comparison to BC in 2008, the sign of error in NEI05 relative to the coastal posterior and that study is consistent. An inventory with sector-specific breakdowns of BC emissions, additional inversions with more thorough speciated local observations, and higher resolution would all be required to investigate sector-specific anthropogenic pollution.

3.4 Error diagnostics

Analysis of posterior emissions uncertainties is useful for understanding the value of the posterior emissions themselves. The diagonal terms of \mathbf{P}^a are the posterior variances, σ_{x_a} , which are always smaller than prior variances. The variance reduction could instead be presented in β space, by utilizing

Eq. (16). However, $\sigma_{\beta^k,i}^2 < \sigma_{\beta^0,i}^2$ is not guaranteed when $x_{a,i} > x_{b,i} = 0$, because the posterior relative emission uncertainty depends on $x_{a,i}$. For this work, the reductions in variance are presented in CV space. The low-rank estimate of \mathbf{P}^a is only valid for linear perturbations away from \mathbf{x}_a . The final outer loop estimate of \mathbf{P}^a is the most accurate, since it is linearized around the state preceding \mathbf{x}_a . A quantitative measure of error reduction in the k_o th outer loop in the i th CV is

$$\rho_{i,k_o} = 1 - \left(\frac{\mathbf{P}_{i,i}^a}{\mathbf{B}_{i,i}} \right)_{k_o} \in [0, 1). \quad (25)$$

Values of ρ_{i,k_o} closer to 1 reflect locations where the observations provide a stronger constraint than the prior. This estimate may not reflect the entire error reduction, since it does not capture potential reductions in previous outer loops. Without propagating updated estimates for \mathbf{B} to subsequent outer loops (e.g., Tshimanga et al., 2008), we also define ρ_{agg} , a qualitative metric that accounts for increases in curvature (decreases in error) in all outer loops:

$$\rho_{i,\text{agg}} = 1 - \prod_{k_o=1}^k \left(\frac{\mathbf{P}_{i,i}^a}{\mathbf{B}_{i,i}} \right)_{k_o} \in [0, 1). \quad (26)$$

$\rho_{i,\text{agg}}$ reveals additional information about observation footprints not shown by $\rho_{i,k_o=6}$. The nonlinear nature of the problem means $\rho_{i,\text{agg}}$ is not quantitative.

Table 5. Total BB emissions for EAs and domain-wide during the 22 and 23/24 June inversions (averaged for a 24 h period). Absolute units are in Mg. Note that the differences (Δ) may not sum due to rounding.

		FINN_STD			QFED_STD			$\frac{\Sigma E_{\text{QFED}}}{\Sigma E_{\text{FINN}}}$	
		ΣE_b	ΣE_a	Δ	ΣE_b	ΣE_a	Δ	b	a
22 Jun	EA1	14	4	-10	82	26	-55	$\times 5.8$	$\times 6.4$
	EA2	6	30	+24	9	15	+6	$\times 1.5$	$\times 0.5$
	EA3	6	4	-2	29	7	-22	$\times 4.5$	$\times 1.6$
	EA4	18	22	+4	52	83	+31	$\times 2.8$	$\times 3.8$
	DOMAIN	59	83	+34	209	171	-38	$\times 3.5$	$\times 2.1$
23+24 Jun	EA1	20	5	-15	70	12	-58	$\times 3.5$	$\times 2.5$
	EA2	28	11	-16	96	29	-67	$\times 3.5$	$\times 2.6$
	EA3	17	12	-5	37	20	-17	$\times 2.2$	$\times 1.7$
	EA4	32	108	+77	107	107	0	$\times 3.4$	$\times 1.0$
	DOMAIN	138	249	+111	471	354	-117	$\times 3.4$	$\times 1.4$

Table 6. Total anthropogenic emissions for EAs and domain-wide during the 22 and 23/24 June inversions (averaged for a 24 h period). The posterior for 23/24 June is from an inversion using both the IMPROVE and ARACTAS-CARB observations. Results shown are for the FINN_STD scenario. Absolute units are in Mg. Note that the differences (Δ) may not sum due to rounding.

	22 Jun			23/24 Jun			$\frac{\Sigma E_{23+24 \text{ Jun}}}{\Sigma E_{22 \text{ Jun}}}$	
	ΣE_b	ΣE_a	Δ	ΣE_b	ΣE_a	Δ	b	a
EA5	5	5	0	7	3	-3	$\times 1.4$	$\times 0.7$
EA6	12	8	-4	17	9	-8	$\times 1.4$	$\times 1.2$
EA7	10	6	-5	16	8	-8	$\times 1.6$	$\times 1.5$
EA8	3	2	-1	5	25	+20	$\times 1.6$	$\times 9.9$
EA9	5	4	-1	6	11	+4	$\times 1.3$	$\times 2.7$
EA10	2	2	0	3	8	+5	$\times 1.4$	$\times 3.7$
DOMAIN	81	68	-13	114	123	+9	$\times 1.4$	$\times 1.8$

Both ($\rho_{k_o=6}$) and ρ_{agg} are presented in Figs. 12 and 13 for the BB and anthropogenic members of \mathbf{x}_a , respectively. Fifty inner loop iterations were taken in the final outer loop to improve ρ estimates. $\rho_{k_o=6}$ is $< 45\%$ across all scenarios, except for QFED_STD BB sources near the IMPROVE sites on 23/24 June. If the inner loop were halted at 10 iterations, the error reduction estimates would be reduced by up to $\sim 10\%$ (i.e., 35 instead of 45%) in the darkest grid cells. The BB error reduction shown in Fig. 12 has similar spatial distributions for FINN_STD and QFED_STD scenarios, but differs significantly between the two time periods due to the different spatial coverage of the observations. The reductions in the north on 22 June are more disperse for QFED_STD, which could be caused by the same regridding errors and plume rise differences that influence the posterior emissions. There is also more error reduction in the south for the QFED_STD emissions. In general, the grid-scale uncertainty improvement is confined to sources close to the observations.

The most obvious application of ρ is to evaluate the footprint of a set of measurements. For example, the large relative BB emission increments in EA1–EA3 on 23/24 June indi-

cate that distant observations can have a large impact on the posterior emissions magnitudes. However, $\rho_{i,k_o=6}$ in Fig. 12 indicates there is nearly zero uncertainty reduction for those emissions. Also, upon considering the last two columns of Table 6, one might conclude that there is a missing weekend (22 June) to weekday (23/24 June) variation in BC emissions within EA8–10. However, Fig. 13 shows that the 22 June observations only weakly reduce uncertainty in emissions.

In a more tangible application, ρ can be used to assess existing and future observing strategies in a similar way to how Yang et al. (2014) used adjoint sensitivity information to plan future meteorological observing sites to improve forecasts of extreme dust events in the Korean Peninsula. Fig. 13 presents anthropogenic ρ for different combinations of surface and aircraft observations on 23/24 June. The surface observations primarily resolve sources near Fresno, and to a lesser extent near Los Angeles. Since the purpose of the IMPROVE network is to measure background concentrations, it is mostly successful on 23 June in not being influenced by anthropogenic sources of BC from the major cities. If the goal were to measure anthropogenic sources, inflows, or domain-wide concentrations on daily timescales, then ρ

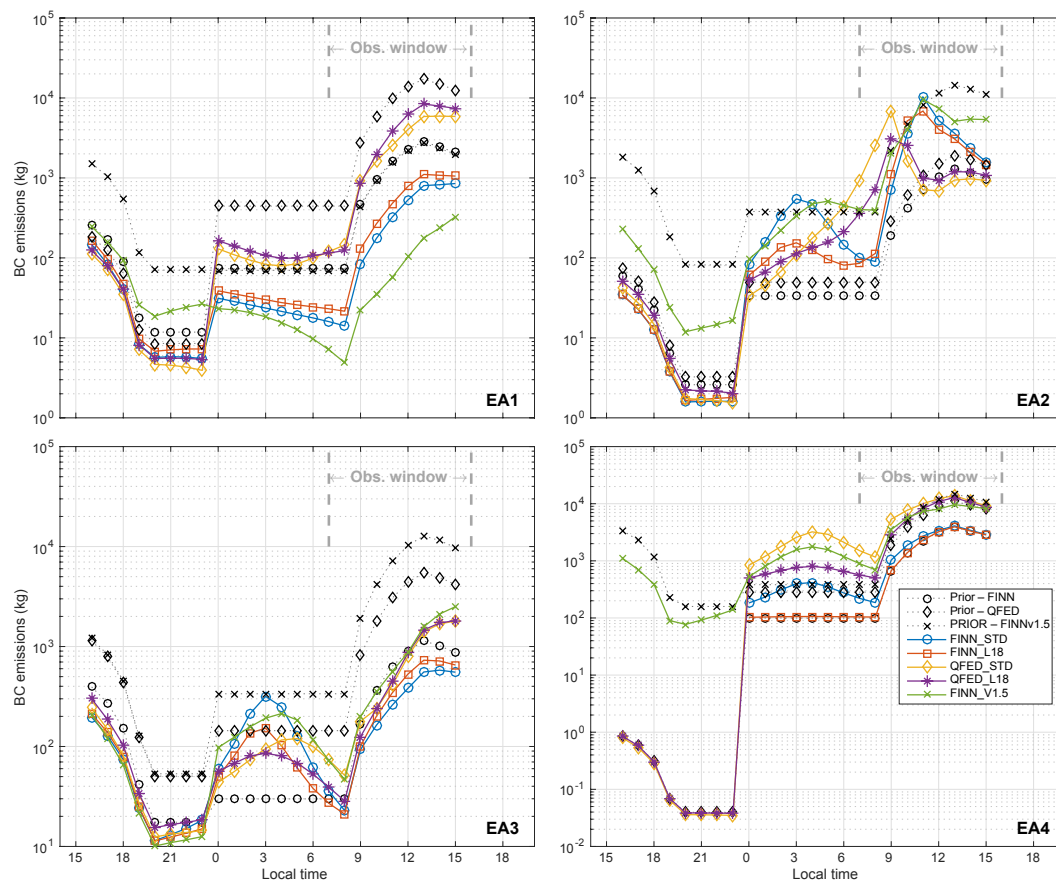


Figure 9. Hourly BB diurnal emission patterns for the four EAs and all inversion scenarios for 22 June, 00:00–23:00 Z, with the time shown in LT. The priors are shown as black lines, while the posteriors from specific inversion scenarios are shown in color. Note that FINNv1.0 did not have any fires in EA4 on 21 June.

would suggest using a different surface network distribution. Such a conclusion does not conflict with the success of using IMPROVE observations to provide top-down constraints on both BB and anthropogenic emissions on monthly timescales (e.g., Mao et al., 2015). That strategy is consistent with what is generally known: further decreasing uncertainty requires observing the same phenomena more thoroughly. For hourly to daily timescales, more observations are needed close to and downwind of chemical sources, and at high spatial and temporal resolution (e.g., from repeated aircraft overpasses, extra aircraft, hourly-average surface sites, or satellites).

Another piece of information useful for comparing observing configurations and inversion scenarios is the trace of the resolution matrix, or degrees of freedom for signal, i.e.,

$$\text{DOF} = \text{Tr} \left[\mathbf{I}_n - \mathbf{P}^a \mathbf{B}^{-1} \right], \quad (27)$$

which is equal to the number of modes of variability in the emissions that are resolved by the observations (Wahba, 1985; Purser and Huang, 1993; Rodgers, 1996).

Substituting the approximation for \mathbf{P}^a from Eq. (23),

$$\begin{aligned} \text{DOF} &\approx n - \text{Tr} \left[\left(\mathbf{B} + \mathbf{U} \left(\sum_{k_i=1}^l (\lambda_{k_i}^{-1} - 1) \hat{\mathbf{v}}_{k_i} \hat{\mathbf{v}}_{k_i}^T \right) \mathbf{U}^T \right) \mathbf{B}^{-1} \right] \\ &\approx - \text{Tr} \left[\mathbf{U} \left(\sum_{k_i=1}^l (\lambda_{k_i}^{-1} - 1) \hat{\mathbf{v}}_{k_i} \hat{\mathbf{v}}_{k_i}^T \right) \mathbf{U}^T \mathbf{B}^{-1} \right]. \end{aligned} \quad (28)$$

Since \mathbf{U} is square, $\mathbf{U}^T \mathbf{B}^{-1} \mathbf{U} = \mathbf{I}_n$, and $\text{Tr} \left[\hat{\mathbf{v}}_{k_i} \hat{\mathbf{v}}_{k_i}^T \right] = \hat{\mathbf{v}}_{k_i}^T \hat{\mathbf{v}}_{k_i} = 1$, the expression simplifies as

$$\begin{aligned} \text{DOF} &= - \text{Tr} \left[\left(\sum_{k_i=1}^l (\lambda_{k_i}^{-1} - 1) \hat{\mathbf{v}}_{k_i} \hat{\mathbf{v}}_{k_i}^T \right) \mathbf{U}^T \mathbf{B}^{-1} \mathbf{U} \right] \\ &\approx \sum_{k_i=1}^l (1 - \lambda_{k_i}^{-1}) \text{Tr} \left[\hat{\mathbf{v}}_{k_i} \hat{\mathbf{v}}_{k_i}^T \right] \\ &\approx \sum_{k_i=1}^l (1 - \lambda_{k_i}^{-1}). \end{aligned} \quad (29)$$

Therefore, the only information needed to compute DOF is the eigenvalues of \mathbf{T}_l . Each inner loop, k_i , has the potential to

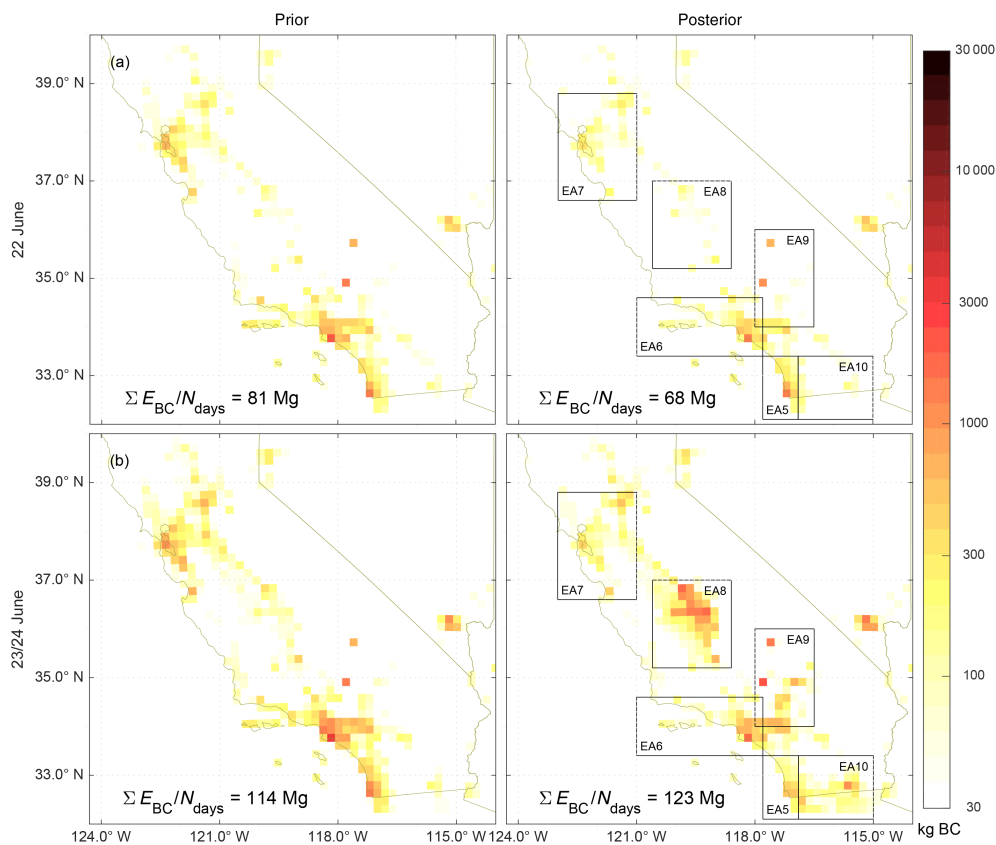


Figure 10. Prior and posterior grid-scale anthropogenic emissions of BC per 24 h for FINN_STD on 22 June, 00:00–23:00 Z (top row) and 23 June, 00:00 Z to 24 June, 23:00 Z. EA5–10 are outlined with black boxes.

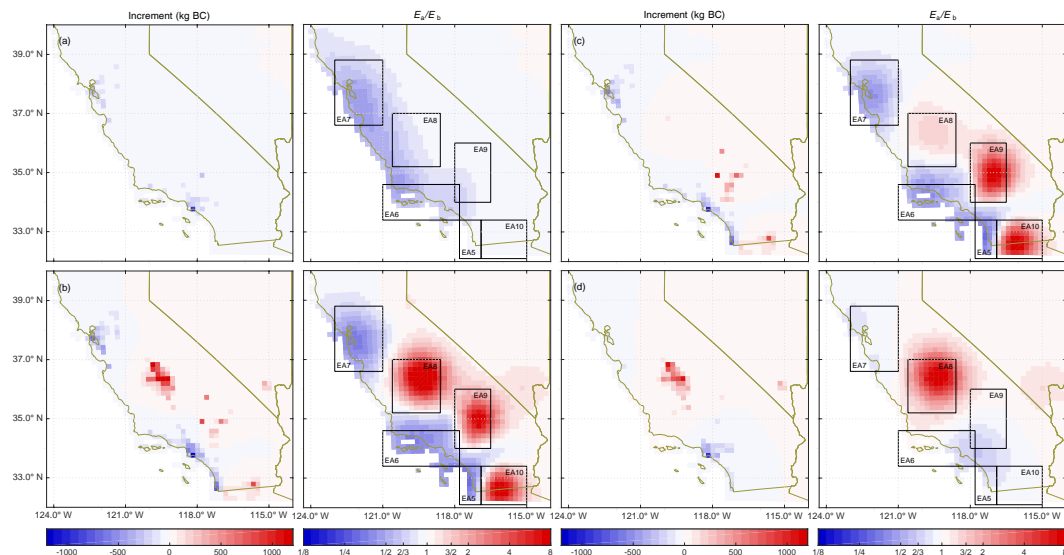


Figure 11. Anthropogenic analysis increment (posterior minus prior) per 24 h and posterior linear scaling factor (β) for the (a) FINN_STD (22), (b) FINN_STD (23/24), (c) ACFT, and (d) SURF inversion scenarios. EA5–9 are outlined with black boxes in the scaling factor plots.

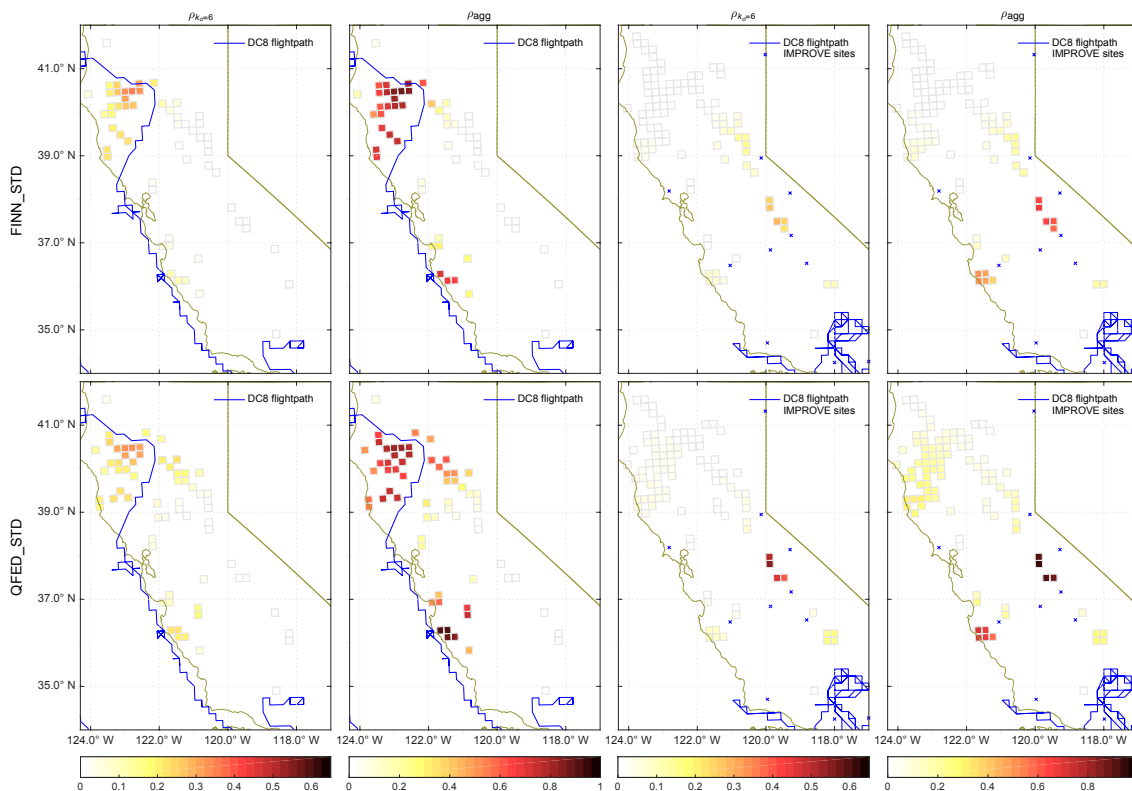


Figure 12. BB error reduction in the final outer loop ($\rho_{k_0=6}$) and aggregated across all outer loops (ρ_{agg}) for the two primary BB scenarios on 22 June 00:00–23:00 Z and 23 June, 00:00 Z–24 June 23:00 Z. The ARCTAS-CARB DC8 flightpath and IMPROVE sites at model grid centers are overlaid.

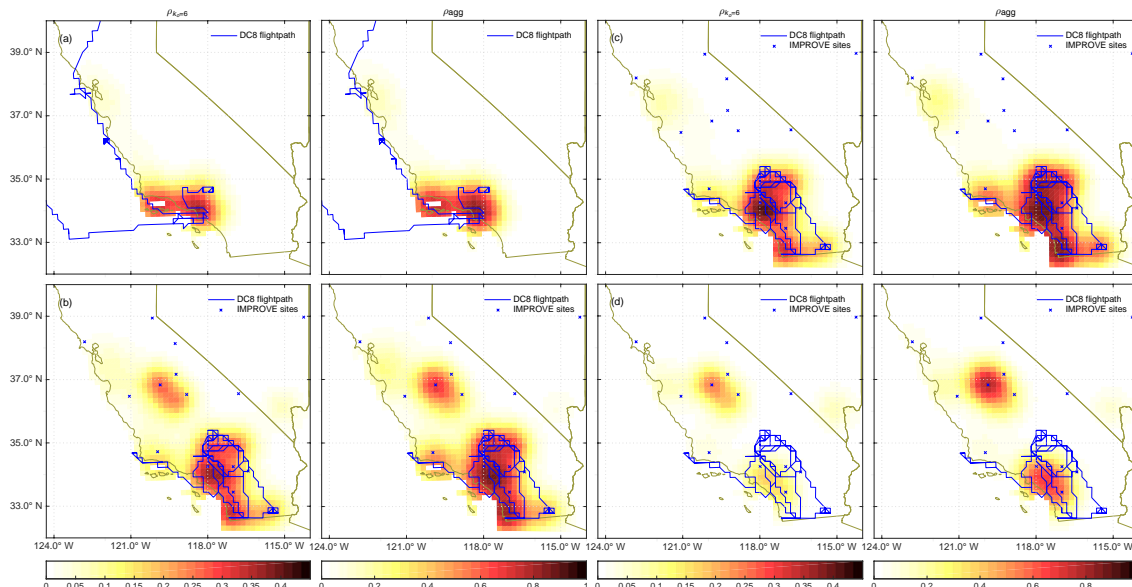


Figure 13. Anthropogenic error reduction in the final outer loop ($\rho_{k_0=6}$) and aggregated across all outer loops (ρ_{agg}) for the (a) FINN_STD (22), (b) FINN_STD (23/24), (c) ACFT, and (d) SURF inversion scenarios. The ARCTAS-CARB DC8 flightpath and IMPROVE sites at model grid centers are overlaid.

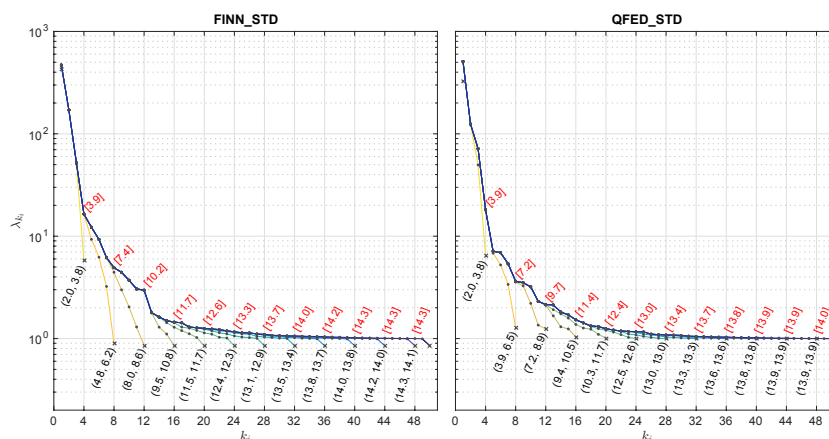


Figure 14. Eigenvalue spectra for FINN_STD and QFED_STD in the final outer loop on 22 June. The lines show the estimate of the spectrum $[\lambda_1, \dots, \lambda_{k_i=l}]$ in every fourth inner loop iteration, l . The black numbers in parentheses are the estimates of DOF that include eigenvalues in the sets (converged to within 5% of the previous estimate, all available). The red numbers in brackets are the truncated estimates of DOF using the most completely converged set of eigenvalues available in the 50th iteration.

constrain one additional mode of variability in the emission scaling factors. For all of our inversion scenarios, the leading eigenvalue is on the order of $10^2 - 10^3$, which is equal to the condition number of the full-rank Hessian. As the Lanczos optimization proceeds, each subsequent λ_{k_i} is smaller, asymptotically approaching unity, and each eigenmode provides less information than the one preceding it about scaling factor variability.

Figure 14 gives three estimates of DOF at each level of truncation in the final outer loop, that is, if higher degrees of eigenvalues were ignored. In that figure, we plot eigenvalue spectra of the FINN_STD and QFED_STD scenarios on 22 June. Similar to ρ , we use a 50-iteration linear optimization to improve the bounds on DOF. The $k_i = l$ estimate of the eigenvalue spectrum at each iteration is represented by a single colored line. Each member of the eigenvalue spectrum, represented by vertical grid lines in Fig. 14, converges toward an upper bound as more iterations are taken. Initial guesses for the least dominant eigenvalues are less than 1 for $k_i \geq 8$ for FINN_STD, but they exceed 1 after an additional iteration, consistent with the properties of the Lanczos sequence. The first DOF value in parentheses adheres to the philosophy that only converged eigenvalues should be used to estimate DOF; it excludes $\lambda_{k_i}, \dots, \lambda_l$ such that λ_{k_i} is more than 5% changed from the previous estimate. The second DOF value in parentheses uses all of the current estimates of the eigenvalues available in iteration l . This is still a conservative estimate of DOF, because the true eigenvalues of the full-rank \mathbf{T}_n are always larger than their current numerical estimate. After enough iterations, the numerical growth in DOF is very small, and further computation is not warranted. As the eigenvalue spectra in Fig. 14 and the cost function reduction in Fig. 3 show, this is long after the cost function is converged enough for practical purposes. The posterior CVs,

which are the primary result from inverse modeling, do not change significantly in the final outer loop. Finally, the best estimates of DOF in red brackets are evaluated at different truncations using the most-converged values of the eigenvalues found in the 22nd iteration.

Similar to ρ , the quantitative application of DOF is limited to the final outer loop, when $\delta \mathbf{x}^n$ is small enough that $(\mathcal{H}_{\delta v})^{-1}|_{\mathbf{x}^{n-1}} \approx (\mathcal{H}_{\delta v})^{-1}|_{\mathbf{x}^n}$. Absent the need to estimate the posterior Hessian, the outer loop could be ended an iteration earlier. In the inner loop, truncated estimates of \mathcal{H}^{-1} and its eigenvalue spectrum at earlier iterations will provide conservative values for both DOF and ρ . The actual DOF value is higher than any value shown in Figs. 14 (22 June) and 15 (23/24 June). Therefore, the 22 June observations constrain > 14 modes of hourly grid-scale variability through 4D-Var in both the FINN_STD and QFED_STD scenarios. Just like for ρ , the optimization constrains additional modes in the earlier outer loop iterations, but that quantification is not straightforward since DOF are defined for linear behavior. If all outer loops were similar, then the total DOF value for the entire nonlinear optimization is on the order of 30 to 40.

As shown in Fig. 15, the DOF values on 23 and 24 June after 50 iterations are 10, 17, and 23 for the SURF, ACFT, and FINN_STD(23/24) scenarios, respectively. The relative magnitudes show that using combined surface and aircraft observations provides an additional value over using either independently, although the two platforms might have some redundancy. This conclusion is consistent with the maps of BB and anthropogenic ρ in Fig. 13, where the footprints of SURF and ACFT have slight overlap near Los Angeles, but are otherwise independent. Additionally, the higher DOF value of ACFT is consistent with its more widespread and larger magnitude ρ values. The slower eigenvalue convergence when

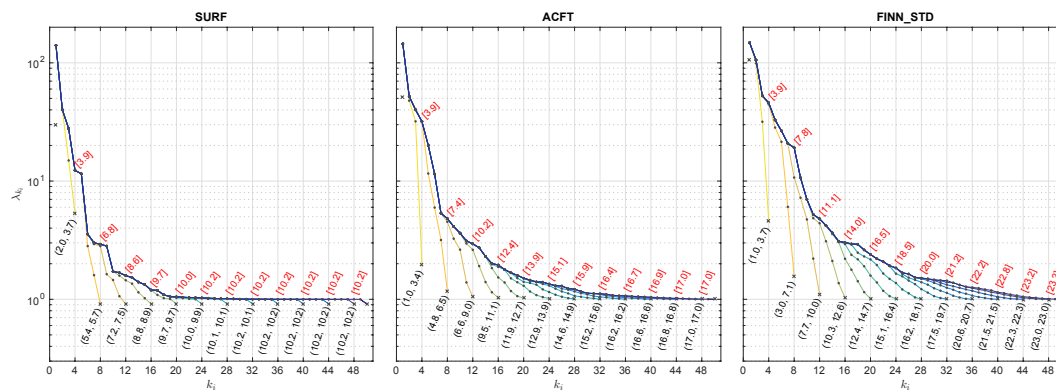


Figure 15. Eigenvalue spectra for SURF, ACFT, and SURF+ACFT in the final outer loop on 23 and 24 June. The lines show the estimate of the spectrum $[\lambda_1, \dots, \lambda_{k_i=l}]$ in every fourth inner loop iteration, l . The black numbers in parentheses are the estimates of DOF that include eigenvalues in the sets (converged to within 5% of the previous estimate, all available). The red numbers in brackets are the truncated estimates of DOF using the most completely converged set of eigenvalues available in the 50th iteration.

both observing types are utilized means that additional inner iterations could yield higher estimates for DOF in that case. What is even more clear, and intuitive, is that ρ and DOF estimates require more iterations as the number of constrained CVs increases, which is directly dependent on the number of observations. The sparse ρ map for SURF in Fig. 13 and the large spike near Fresno illustrate that while near-source surface measurements can be a powerful constraint, measurements of background concentrations provide relatively little constraints to characterize CA anthropogenic emissions on 1-day timescales.

3.5 Cross-validation

As an additional evaluation of the robustness of the emission scaling factors, we apply them in cross-validation tests. In two separate evaluations, the 22 June scaling factors are applied to 23–26 June emissions, and the 23/24 June scaling factors are applied to 25–26 June emissions. The heterogeneous adjoint sensitivity signs and magnitudes for each source sector we found on each day of the campaign (Guerrette and Henze, 2015) are an indication that corrective scaling factors in each day will be unique. In that work, we found that the 24 June observations were most sensitive to southern California anthropogenic sources on 24 June and to northern and southern California coastal sources of both sectors on 23 June. The 26 June observations were most sensitive to northern California fires, and the adjoint sensitivities were of opposite sign than on 23 and 24 June.

As shown in Fig. 4, the cross-validated 22 June scaling factors rarely generate improvements to model performance, when compared to 24 and 26 June aircraft observations. On 24 June, some of the high bias predictions are corrected, or even over-compensated, but the low bias prior locations are unaffected. Table 2 shows the R^2 and slope of the linear trend lines. The scatter of the fit for QFED_STD on 24 June

and the slope for FINN_STD on 26 June are slightly improved, but all other metrics degrade. The increase in slope for FINN_STD comes as a result of better fit to very large concentrations above the PBL associated with fire sources on multiple previous days. The posterior scaling factors generated from the 23/24 June inversion degrade the forecast of aircraft measurements on 26 June. Since the posterior primarily serves to reduce coastal anthropogenic and BB emissions, it is not surprising that it does not improve a low bias prior 2 days later.

Table 3 includes cross-validated surface measurements on 23 June and 26 June. There is very little change to the modeled surface concentrations as a result of posterior scaling factors derived from inversions that only use aircraft observations. Assimilating surface observations on 23 June (Monday) does improve model comparisons to surface observations on 26 June (Thursday). Those small improvements imply that errors are weakly correlated between weekdays. Although it is beyond the information content provided by the observations used in this work, future studies could compare the efficacy of using weak multiday correlation in **B** and the hard constraint of 24 h periodic scaling factors used herein. Aircraft and surface observations do not appear to be useful for cross-validation of each other over the short timescales and limited set of flights considered here. At least for this study period, when they are not collocated, each provides some unique information to the inversion.

4 Conclusions and future work

We have presented the implementation and an application of incremental chemical 4D-Var using an atmospheric chemistry model with online meteorology in WRFDA-Chem. This work expands on our previous efforts to develop the ADM and TLM in WRFPLUS-Chem (Guerrette and Henze, 2015). This new inversion tool takes advantage of previous de-

velopments of meteorological data assimilation in WRFDA (Barker et al., 2005; Huang et al., 2009). That same framework is applied to log-normally distributed emission scaling factors through an exponential transform. We utilize the square root preconditioner for a CVT using horizontal and temporal scaling factor correlations. The Lanczos linear optimization algorithm in the inner loop allows for estimation of posterior error and DOF for objectively evaluating observing systems. Outer loop convergence is improved with a heuristic DGN multiplier, which allows the incremental framework to handle the nonlinearity of the log-normal cost function. While the optimizations herein focus exclusively on emissions, which are known to be important drivers of model uncertainty in BC estimates (e.g., Fu et al., 2012; F. Zhang et al., 2014), other factors such as meteorology, plume rise and deposition mechanisms may also affect the model's predictions of BC concentrations.

When applied to the ARCTAS-CARB campaign period, it is not clear which prior emissions perform better. If assessment by initial cost function value alone were meaningful, FINNv1.0 performs best. However, that could be due to FINNv1.0 being biased low combined with the assumption of Gaussian distributed model–observation errors. Positive residuals are weighted higher than negative ones, even when relative errors are equal. There could be some improvement to the posterior emissions by implementing the incremental log-normal methods of Fletcher and Jones (2014) or Song et al. (2016). If the purpose of the inventory is to provide air quality warnings to the major California cities, then FINNv1.0, FINNv1.5, and QFEDv2.4r8 all have some built-in high bias that will err on the side of caution. Their inability to reproduce high concentrations near sources points to either a deficiency in the inventories, vertical mixing processes, or the temporal observation averaging procedure followed herein, diagnosis of which would require measurements of plume injection heights and widths. The relative magnitudes of grid-scale fire and anthropogenic emissions make it difficult to simultaneously constrain them without additional information. More work should be done to improve both bottom–up and top–down estimates of anthropogenic emissions outside of fire events. We also agree with Mao et al. (2015), who recommended multi-species inversions (e.g., BC and CO) to discern specific source sectors.

Through the setup and application of the 4D-Var system, we gained valuable knowledge to guide future modeling and measurement efforts. We found two errors in the diurnal distribution of BB emissions and identified a scaling necessary to apply QFED to the western US. Additionally, the highly heterogeneous posterior scaling factors during ARCTAS-CARB raise questions that the limited BB observations during that time period do not answer. (1) Are BB emission errors always heterogeneous, or only during a transient initiation stage like that observed in June 2008? If heterogeneity is consistent outside initiation events, then inversions should apply weaker inter-day correlation than the hard

constraint used herein or have independent scaling factors for each day. (2) Are the temporally bimodal posterior emissions realistic, or are they an artifact of the correlation timescale used? (3) Are the BB plume heights reasonable, and should they follow a diurnal pattern? The current 1-D plume rise mechanism in WRF-Chem depends strongly on specified burned areas, which are diurnally invariant and highly uncertain (e.g., Boschetti et al., 2004). The last two questions indicate that there is value in continuous night (between 20:00 and 06:00 LT) and day measurements of the same fire region. Since models poorly predict shallow boundary layers, the use of nighttime observations in 4D-Var would require characterization and subsequent model tuning of those vertical mixing processes. Furthermore, if it is accepted that high-resolution models are required to accurately predict degraded air quality events, then high spatial and/or temporal resolution concentration measurements from research campaigns or geostationary satellites are necessary to provide the sufficient constraints on inventory errors. The error reduction estimation method provided herein will be useful for planning these future missions.

Future applications of the WRFDA-Chem system developed here may consider improvements such as the following. One possible way to reduce model uncertainty would be to extend the multi-incremental 4D-Var available in WRFDA (X. Zhang et al., 2014) to the new scaling factor CVs. Multi-incremental chemical 4D-Var would use a high-resolution model forecast to generate trajectory checkpoint files (see Guerrette and Henze, 2015), and could take advantage of improvements to chemical transport at higher resolution realized by using online meteorology demonstrated by Grell et al. (2004) and Grell and Baklanov (2011). In addition, four-dimensional data assimilation (FDDA) nudging has been shown to improve wind fields and was used successfully in an LPDM emission inversion (Lauvaux et al., 2016). Even after exhausting methods to improve the posterior, the error contributions from hard-coded descriptions of meteorology can be bounded using ensemble and sensitivity tests (e.g., Angevine et al., 2014; Lauvaux et al., 2016).

Data availability. Single-particle soot photometer measurements of total black carbon mass during ARCTAS-CARB are available at <https://www-air.larc.nasa.gov/cgi-bin/ArcView/arctas#KONDO.YUTAKA/> (Sahu et al., 2012). Total elemental carbon mass measurements taken by thermal optical reflectance at IMPROVE network sites are available at <http://views.cira.colostate.edu/fed/DataWizard/Default.aspx> (Malm et al., 1994). The FINN and QFED biomass burning emissions can be found at <http://bai.acom.ucar.edu/Data/fire/> (Wiedinmyer et al., 2006, 2011) and <ftp://ftp.nccs.nasa.gov/aerosol/emissions/QFED/v2.4r8/0.1/> (Darmenov and da Silva, 2015), respectively. Information at <https://ruc.noaa.gov/wrf/wrf-chem/> (Grell et al., 2005) describes how to utilize NEI tabulated anthropogenic source magnitudes and the biomass burning emissions with WRF-Chem.

Appendix A: Relating DA and optimization formulations

The linear optimization in the inner loop solves a system

$$\begin{aligned} \min_{\hat{\mathbf{x}}} F(\hat{\mathbf{x}}) &= \frac{1}{2} \hat{\mathbf{x}}^\top \mathbf{A}' \hat{\mathbf{x}} - \hat{\mathbf{x}}^\top \mathbf{b} + c \\ \mathbf{A}' \hat{\mathbf{x}} &= \mathbf{b}. \end{aligned} \quad (\text{A1})$$

In our case, $\hat{\mathbf{x}} \equiv \delta \mathbf{v}^k$. The equivalence of Eqs. (7) and (A1) is apparent in Tshimanga et al. (2008), who provide a notational translation between publications on DA and those on minimization algorithms and preconditioners. We repeat their translation to account for the differences in formulation of Eqs. (7) and (5) in Tshimanga et al. (2008).

The process starts by considering Lawless et al. (2005) and Gratton et al. (2007), who show that incremental 4D-Var is equivalent to a truncated Gauss–Newton (TGN) optimization algorithm. The incremental 4D-Var cost function is condensed to

$$\min_{\delta \mathbf{v}} J(\delta \mathbf{v}) = \frac{1}{2} \mathbf{f}(\delta \mathbf{v})^\top \mathbf{f}(\delta \mathbf{v}), \quad (\text{A2})$$

where

$$\mathbf{f}(\delta \mathbf{v}^k) \equiv \left(\mathbf{R}^{-\frac{1}{2}} \left(\mathbf{G}^{k-1} \mathbf{U} \delta \mathbf{v}^k - \mathbf{d}^{o,k-1} \right) \right). \quad (\text{A3})$$

This definition of \mathbf{f} is what enables incremental 4D-Var to be characterized as TGN. The remainder of the derivation amounts to substitutions. GN approximates Newton's method in each quadratic minimization problem, k , to solve for the increment $\delta \mathbf{v}^k$ in the linearized system

$$\mathcal{H}_{\delta \mathbf{v}} \delta \mathbf{v}^k = -\nabla J. \quad (\text{A4})$$

This form is equivalent to multiplying Eq. (10) by the Hessian on both sides. In our case, the right-hand side is $\mathbf{b} \equiv -\nabla J = -\mathbf{F}^{k-1 \top} \mathbf{f}(\delta \mathbf{v}^{k-1})$, where

$$\mathbf{f}(\delta \mathbf{v}^{k-1}) \equiv - \left(\mathbf{R}^{-\frac{1}{2}} \mathbf{d}^{o,k-1} \right), \quad (\text{A5})$$

and

$$\mathbf{F}^{k-1} \equiv \nabla_{\delta \mathbf{v}^{k-1}} \mathbf{f}^l|_{\delta \mathbf{v}^{k-1}} = \left(\mathbf{R}^{-\frac{1}{2}} \mathbf{G}^{k-1} \mathbf{U} \right). \quad (\text{A6})$$

$\mathbf{f}(\delta \mathbf{v}^{k-1})$ and its Jacobian are fixed for each outer loop by the $k-1$ trajectory. Completing the GN algorithm, the Hessian ($\mathcal{H}_{\delta \mathbf{v}}$) is approximated by $\mathbf{A}' \equiv \mathbf{F}^{k-1 \top} \mathbf{F}^{k-1}$, after ignoring mixed partial derivatives of \mathbf{f} . The Hessian of Eq. (A2) matches that of Eq. (7), namely

$$\mathcal{H}_{\delta \mathbf{v}} = \mathbf{I}_n + \mathbf{U}^\top \mathbf{G}^{k-1 \top} \mathbf{R}^{-1} \mathbf{G}^{k-1} \mathbf{U}. \quad (\text{A7})$$

After substitutions, Eq. (A4) becomes

$$\mathbf{F}^{k-1 \top} \mathbf{F}^{k-1} \delta \mathbf{v}^k = -\mathbf{F}^{k-1 \top} \mathbf{f}(\delta \mathbf{v}^{k-1}), \quad (\text{A8})$$

which expands to

$$\begin{aligned} & \left(\mathbf{I}_n + \mathbf{U}^\top \mathbf{G}^{k-1 \top} \mathbf{R}^{-1} \mathbf{G}^{k-1} \mathbf{U} \right) \delta \mathbf{v}^k \\ &= \mathbf{d}^{b,k-1} + \mathbf{U}^\top \mathbf{G}^{k-1 \top} \mathbf{R}^{-1} \mathbf{d}^{o,k-1}. \end{aligned} \quad (\text{A9})$$

Solving for $\delta \mathbf{v}^k$ gives the same update formula that would result from setting Eq. (9) equal to zero,

$$\begin{aligned} \delta \mathbf{v}^k &= \left(\mathbf{I}_n + \mathbf{U}^\top \mathbf{G}^{k-1 \top} \mathbf{R}^{-1} \mathbf{G}^{k-1} \mathbf{U} \right)^{-1} \\ & \left(\mathbf{d}^{b,k-1} + \mathbf{U}^\top \mathbf{G}^{k-1 \top} \mathbf{R}^{-1} \mathbf{d}^{o,k-1} \right). \end{aligned} \quad (\text{A10})$$

Thus, by defining \mathbf{f} appropriately, the equivalence between GN and incremental 4D-Var is verified.

Appendix B: Derivation of the truncated inverse Hessian

After l inner iterations, the Lanczos vectors form an orthogonal matrix, $\mathbf{Q}_l = [\hat{\mathbf{q}}_1, \dots, \hat{\mathbf{q}}_l]$, which satisfies

$$\mathcal{H}_{\delta \mathbf{v}} \mathbf{Q}_l = \mathbf{Q}_l \mathbf{T}_l. \quad (\text{B1})$$

The extremal eigenvalues of \mathbf{T}_l are good approximations to $\mathcal{H}_{\delta \mathbf{v}}$'s extremal eigenvalues (Golub and Van Loan, 1996). \mathbf{T}_l can be decomposed as

$$\mathbf{T}_l = \mathbf{W}_l \mathbf{\Lambda}_l \mathbf{W}_l^{-1}. \quad (\text{B2})$$

If we were to carry out the minimization for n steps, we would find all the Lanczos vectors, and would be able to construct the full \mathbf{T} and \mathbf{Q} matrices. In that case, the orthogonal Lanczos vectors admit $\mathbf{Q}\mathbf{Q}^\top = \mathbf{I}$. When combined with Eq. (B1),

$$\mathcal{H}_{\delta \mathbf{v}} = \mathbf{Q}\mathbf{W}\mathbf{\Lambda}\mathbf{W}^{-1}\mathbf{Q}^\top. \quad (\text{B3})$$

Because the eigenvectors are orthonormal,

$$\mathcal{H}_{\delta \mathbf{v}} = (\mathbf{Q}\mathbf{W}) \mathbf{\Lambda} (\mathbf{Q}\mathbf{W})^\top. \quad (\text{B4})$$

Thus, the eigenvectors of $\mathcal{H}_{\delta \mathbf{v}}$ are approximately equal to the normalized eigenvectors of \mathbf{T} , premultiplied by the matrix of Lanczos vectors, i.e.,

$$\mathcal{H}_{\delta \mathbf{v}} = \hat{\mathbf{v}} \mathbf{\Lambda} \hat{\mathbf{v}}^\top, \quad (\text{B5})$$

where the k_i th eigenvector of $\mathcal{H}_{\delta \mathbf{v}}$ is

$$\hat{\mathbf{v}}_{k_i} = \mathbf{Q} \hat{\mathbf{w}}_{k_i}. \quad (\text{B6})$$

The Hessian is constructed by

$$\mathcal{H}_{\delta v} = \hat{\mathbf{v}} \mathbf{\Lambda} \hat{\mathbf{v}}^\top = \sum_{k_i=1}^n \lambda_{k_i} \hat{\mathbf{v}}_{k_i} \hat{\mathbf{v}}_{k_i}^\top. \quad (\text{B7})$$

Since the Hessian and its inverse have identical eigenvectors and reciprocal eigenvalues, the inverse is

$$[\mathcal{H}_{\delta v}]^{-1} = \sum_{k_i=1}^n \lambda_{k_i}^{-1} \hat{\mathbf{v}}_{k_i} \hat{\mathbf{v}}_{k_i}^\top. \quad (\text{B8})$$

Although this expression is usable, computational resource limitations require $l \ll n$. Truncating the sum yields a low rank estimate for the inverse, and for the posterior error which it estimates.

A more robust estimate of the posterior error is a low-rank update to the full-rank prior covariance, \mathbf{B} . To pursue that goal, first we return to the linear algebra formula, and then add and subtract the identity matrix to get

$$\begin{aligned} \mathcal{H}_{\delta v} &= \mathbf{I} + \hat{\mathbf{v}} \mathbf{\Lambda} \hat{\mathbf{v}}^\top - \mathbf{I} \\ &= \mathbf{I} + \hat{\mathbf{v}} \mathbf{\Lambda} \hat{\mathbf{v}}^\top - \hat{\mathbf{I}} \hat{\mathbf{I}}^\top \\ &= \mathbf{I} + \sum_{k_i=1}^n (\lambda_{k_i} - 1) \hat{\mathbf{v}}_{k_i} \hat{\mathbf{v}}_{k_i}^\top. \end{aligned} \quad (\text{B9})$$

Now we repeat the truncation,

$$\mathcal{H}_{\delta v} \approx \mathbf{I} + \sum_{k_i=1}^l (\lambda_{k_i} - 1) \hat{\mathbf{v}}_{k_i} \hat{\mathbf{v}}_{k_i}^\top, \quad (\text{B10})$$

where $\hat{\mathbf{v}}_{k_i}$ is constructed from the partial set of Lanczos vectors as

$$\hat{\mathbf{v}}_{k_i} = \mathbf{Q}_l \hat{\mathbf{w}}_{lk_i}. \quad (\text{B11})$$

Next we apply the Sherman–Morrison formula to recursively build the inverse for each term in the sum. Throughout, we will take advantage of the following two relationships for orthogonal vectors:

$$\hat{\mathbf{v}}_j^\top \hat{\mathbf{v}}_j = 1$$

and

$$\hat{\mathbf{v}}_j^\top \hat{\mathbf{v}}_i = 0; \quad j \neq i.$$

Starting with the first term,

$$\begin{aligned} \mathbf{N}_1^{-1} &= \left[\mathbf{I} + (\lambda_1 - 1) \hat{\mathbf{v}}_1 \hat{\mathbf{v}}_1^\top \right]^{-1} \\ &= \mathbf{I}^{-1} - \frac{\mathbf{I}^{-1} (\lambda_1 - 1) \hat{\mathbf{v}}_1 \hat{\mathbf{v}}_1^\top \mathbf{I}^{-1}}{1 + (\lambda_1 - 1) \hat{\mathbf{v}}_1^\top \mathbf{I}^{-1} \hat{\mathbf{v}}_1} \\ &= \mathbf{I} - \frac{(\lambda_1 - 1) \hat{\mathbf{v}}_1 \hat{\mathbf{v}}_1^\top}{\lambda_1} \\ &= \mathbf{I} + (\lambda_1^{-1} - 1) \hat{\mathbf{v}}_1 \hat{\mathbf{v}}_1^\top. \end{aligned}$$

This result fits our desired proof. Now, for the second term,

$$\begin{aligned} \mathbf{N}_2^{-1} &= \left\{ \mathbf{N}_1 + (\lambda_2 - 1) \hat{\mathbf{v}}_2 \hat{\mathbf{v}}_2^\top \right\}^{-1} \\ &= \mathbf{N}_1^{-1} - \frac{\mathbf{N}_1^{-1} (\lambda_2 - 1) \hat{\mathbf{v}}_2 \hat{\mathbf{v}}_2^\top \mathbf{N}_1^{-1}}{1 + (\lambda_2 - 1) \hat{\mathbf{v}}_2^\top \mathbf{N}_1^{-1} \hat{\mathbf{v}}_2} \\ &= \mathbf{I} + (\lambda_1^{-1} - 1) \hat{\mathbf{v}}_1 \hat{\mathbf{v}}_1^\top - \\ &\quad \frac{\left[\mathbf{I} + (\lambda_1^{-1} - 1) \hat{\mathbf{v}}_1 \hat{\mathbf{v}}_1^\top \right] (\lambda_2 - 1) \hat{\mathbf{v}}_2 \hat{\mathbf{v}}_2^\top \left[\mathbf{I} + (\lambda_1^{-1} - 1) \hat{\mathbf{v}}_1 \hat{\mathbf{v}}_1^\top \right]}{1 + (\lambda_2 - 1) \hat{\mathbf{v}}_2^\top \left[\mathbf{I} + (\lambda_1^{-1} - 1) \hat{\mathbf{v}}_1 \hat{\mathbf{v}}_1^\top \right] \hat{\mathbf{v}}_2} \\ &= \mathbf{I} + (\lambda_1^{-1} - 1) \hat{\mathbf{v}}_1 \hat{\mathbf{v}}_1^\top + (\lambda_2^{-1} - 1) \hat{\mathbf{v}}_2 \hat{\mathbf{v}}_2^\top. \end{aligned}$$

The dot products of orthogonal vectors cancels all terms in the numerator and denominator except the ones multiplied by the identity matrix. The same simplification applies to each additional sum, where the full sum can be expressed as

$$\begin{aligned} \mathbf{N}_l^{-1} &= \mathbf{I} + (\lambda_1^{-1} - 1) \hat{\mathbf{v}}_1 \hat{\mathbf{v}}_1^\top - \\ &\quad \sum_{k_i=2}^l \frac{\left[\mathbf{I} + \sum_{r=1}^{k_i-1} (\lambda_r^{-1} - 1) \hat{\mathbf{v}}_r \hat{\mathbf{v}}_r^\top \right] (\lambda_{k_i} - 1) \hat{\mathbf{v}}_{k_i} \hat{\mathbf{v}}_{k_i}^\top \left[\mathbf{I} + \sum_{r=1}^{k_i-1} (\lambda_r^{-1} - 1) \hat{\mathbf{v}}_r \hat{\mathbf{v}}_r^\top \right]}{1 + (\lambda_{k_i} - 1) \hat{\mathbf{v}}_{k_i}^\top \left[\mathbf{I} + \sum_{r=1}^{k_i-1} (\lambda_r^{-1} - 1) \hat{\mathbf{v}}_r \hat{\mathbf{v}}_r^\top \right] \hat{\mathbf{v}}_{k_i}}. \end{aligned}$$

Here, again, all of the terms where $r \neq k_i$ cancel. What remains is similar to Eq. (B8), but slightly modified.

$$[\mathcal{H}_{\delta v}]^{-1} \approx \mathbf{I} + \sum_{k_i=1}^l (\lambda_{k_i}^{-1} - 1) \hat{\mathbf{v}}_{k_i} \hat{\mathbf{v}}_{k_i}^\top. \quad (\text{B12})$$

After a left-side multiplication by \mathbf{U} and a right-side multiplication by \mathbf{U}^\top , we achieve the desired low rank update to \mathbf{B} found in Eq. (23).

Author contributions. J. J. Guerrette developed the software and ran simulations following the guidance of the principal investigator, D. K. Henze. Both authors contributed to writing and analysis.

Competing interests. The authors declare that they have no conflict of interest.

Acknowledgements. Thank you to two anonymous referees for their constructive and helpful comments that strengthened this work. This research has been supported by a grant from the US Environmental Protection Agency's Science to Achieve Results (STAR) program. Although the research described in the article has been funded wholly or in part by the US Environmental Protection Agency's STAR program through grant R835037, it has not been subjected to any EPA review and therefore does not necessarily reflect the views of the agency, and no official endorsement should be inferred. In addition, this paper is a result of research funded by the National Oceanic and Atmospheric Administration's Earth System Research Laboratory as part of the Fire Influence on Regional and Global Environments Experiment (FIREX) through the grant NOAA NA16OAR4310113. We are thankful for the ARCTAS mission, which was supported by NASA. We thank Y. Kondo for making the SP2 observations available through the NASA LaRC Airborne Science Data for Atmospheric Composition database. We acknowledge the use of FIRMS data from the Land Atmosphere Near-real time Capability for EOS (LANCE) system operated by the NASA/GSFC/Earth Science Data and Information System (ESDIS) with funding provided by NASA/HQ.

Edited by: F. Yu

Reviewed by: three anonymous referees

References

- Andela, N., Kaiser, J. W., van der Werf, G. R., and Wooster, M. J.: New fire diurnal cycle characterizations to improve fire radiative energy assessments made from MODIS observations, *Atmos. Chem. Phys.*, 15, 8831–8846, <https://doi.org/10.5194/acp-15-8831-2015>, 2015.
- Angevine, W. M., Eddington, L., Durkee, K., Fairall, C., Bianco, L., and Brioude, J.: Meteorological Model Evaluation for CalNex 2010, *Mon. Weather Rev.*, 140, 3885–3906, <https://doi.org/10.1175/MWR-D-12-00042.1>, 2012.
- Angevine, W. M., Brioude, J., McKeen, S., and Holloway, J. S.: Uncertainty in Lagrangian pollutant transport simulations due to meteorological uncertainty from a mesoscale WRF ensemble, *Geosci. Model Dev.*, 7, 2817–2829, <https://doi.org/10.5194/gmd-7-2817-2014>, 2014.
- Barker, D., Lee, M.-S., Guo, Y.-R., Huang, W., Huang, H., and Rizvi, Q.: WRF-Var - A unified 3/4D-Var variational data assimilation system for WRF, in: Sixth WRF/15th MM5 Users' Workshop, p. 17, Boulder, CO, NCAR, <http://www2.mmm.ucar.edu/wrf/users/workshops/WS2005/presentations/session10/1-Barker.pdf> (last access: 20 February 2015), 2005.
- Barker, D. M., Huang, W., Guo, Y.-R., Bourgeois, A. J., and Xiao, Q. N.: A three-dimensional variational data assimilation system for MM5: Implementation and initial results, *Mon. Weather Rev.*, 132, 897–914, [http://journals.ametsoc.org/doi/abs/10.1175/1520-0493\(2004\)132<0897:ATVDAS>2.0.CO;2](http://journals.ametsoc.org/doi/abs/10.1175/1520-0493(2004)132<0897:ATVDAS>2.0.CO;2) (last access: 1 May 2016), 2004.
- Bergamaschi, P., Frankenberg, C., Meirink, J. F., Krol, M., Villani, M. G., Houweling, S., Dentener, F., Dlugokencky, E. J., Miller, J. B., Gatti, L. V., Engel, A., and Levin, I.: Inverse modeling of global and regional CH₄ emissions using SCIAMACHY satellite retrievals, *J. Geophys. Res.*, 114, 1–28, <https://doi.org/10.1029/2009JD012287>, 2009.
- Bond, T. C., Doherty, S. J., Fahey, D. W., Forster, P. M., Berntsen, T., DeAngelo, B. J., Flanner, M. G., Ghan, S., Kärcher, B., Koch, D., Kinne, S., Kondo, Y., Quinn, P. K., Sarofim, M. C., Schultz, M. G., Schulz, M., Venkataraman, C., Zhang, H., Zhang, S., Bellouin, N., Guttikunda, S. K., Hopke, P. K., Jacobson, M. Z., Kaiser, J. W., Klimont, Z., Lohmann, U., Schwarz, J. P., Shindell, D., Storelvmo, T., Warren, S. G., and Zender, C. S.: Bounding the role of black carbon in the climate system: A scientific assessment: BLACK CARBON IN THE CLIMATE SYSTEM, *J. Geophys. Res.-Atmos.*, 118, 5380–5552, <https://doi.org/10.1002/jgrd.50171>, 2013.
- Boschetti, L., Eva, H. D., Brivio, P. A., and Grégoire, J. M.: Lessons to be learned from the comparison of three satellite-derived biomass burning products, *Geophys. Res. Lett.*, 31, L21501, <https://doi.org/10.1029/2004GL021229>, 2004.
- Brioude, J., Angevine, W. M., Ahmadov, R., Kim, S.-W., Evan, S., McKeen, S. A., Hsie, E.-Y., Frost, G. J., Neuman, J. A., Pollock, I. B., Peischl, J., Ryerson, T. B., Holloway, J., Brown, S. S., Nowak, J. B., Roberts, J. M., Wofsy, S. C., Santoni, G. W., Oda, T., and Trainer, M.: Top-down estimate of surface flux in the Los Angeles Basin using a mesoscale inverse modeling technique: assessing anthropogenic emissions of CO, NO_x and CO₂ and their impacts, *Atmos. Chem. Phys.*, 13, 3661–3677, <https://doi.org/10.5194/acp-13-3661-2013>, 2013.
- Chen, Y. and Oliver, D. S.: Levenberg–Marquardt forms of the iterative ensemble smoother for efficient history matching and uncertainty quantification, *Comput. Geosci.*, 17, 689–703, <https://doi.org/10.1007/s10596-013-9351-5>, 2013.
- Courtier, P., Thépaut, J.-N., and Hollingsworth, A.: A strategy for operational implementation of 4D-Var, using an incremental approach, *Q. J. Roy. Meteor. Soc.*, 120, 1367–1387, <https://doi.org/10.1002/qj.49712051912>, 1994.
- Cui, Y. Y., Brioude, J., McKeen, S. A., Angevine, W. M., Kim, S.-W., Frost, G. J., Ahmadov, R., Peischl, J., Bousserez, N., Liu, Z., Ryerson, T. B., Wofsy, S. C., Santoni, G. W., Kort, E. A., Fischer, M. L., and Trainer, M.: Top-down estimate of methane emissions in California using a mesoscale inverse modeling technique: The South Coast Air Basin: Inverse Estimate of Methane Emissions, *J. Geophys. Res.-Atmos.*, 120, 6698–6711, <https://doi.org/10.1002/2014JD023002>, 2015.
- Darmenov, A. S. and da Silva, A.: The Quick Fire Emissions Dataset (QFED): Documentation of versions 2.1, 2.2, and 2.4, Tech. Rep. NASA TM-2015-104606/Vol 38, NASA, <https://gmao.gsfc.nasa.gov/pubs/docs/Darmenov796.pdf> (last access: 1 May 2017), 2015 (data available at: <ftp://ftp.nccs.nasa.gov/aerosol/emissions/QFED/v2.4r8/0.1/>, last access: 5 June 2017).

- Elbern, H., Strunk, A., Schmidt, H., and Talagrand, O.: Emission rate and chemical state estimation by 4-dimensional variational inversion, *Atmos. Chem. Phys.*, 7, 3749–3769, <https://doi.org/10.5194/acp-7-3749-2007>, 2007.
- Fisher, M. and Courtier, P.: Estimating the covariance matrices of analysis and forecast error in variational data assimilation, Tech. Rep. Technical Memorandum 220, European Centre for Medium-Range Weather Forecasts, 1995.
- Fletcher, S. J. and Jones, A. S.: Multiplicative and Additive Incremental Variational Data Assimilation for Mixed Lognormal–Gaussian Errors, *Mon. Weather Rev.*, 142, 2521–2544, <https://doi.org/10.1175/MWR-D-13-00136.1>, 2014.
- Fletcher, S. J. and Zupanski, M.: Implications and impacts of transforming lognormal variables into normal variables in VAR, *Meteorol. Z.*, 16, 755–765, <https://doi.org/10.1127/0941-2948/2007/0243>, 2007.
- Freitas, S. R., Longo, K. M., Chatfield, R., Latham, D., Silva Dias, M. A. F., Andreae, M. O., Prins, E., Santos, J. C., Gielow, R., and Carvalho Jr., J. A.: Including the sub-grid scale plume rise of vegetation fires in low resolution atmospheric transport models, *Atmos. Chem. Phys.*, 7, 3385–3398, <https://doi.org/10.5194/acp-7-3385-2007>, 2007.
- Freitas, S. R., Longo, K. M., Trentmann, J., and Latham, D.: Technical Note: Sensitivity of 1-D smoke plume rise models to the inclusion of environmental wind drag, *Atmos. Chem. Phys.*, 10, 585–594, <https://doi.org/10.5194/acp-10-585-2010>, 2010.
- Fu, J. S., Hsu, N. C., Gao, Y., Huang, K., Li, C., Lin, N.-H., and Tsay, S.-C.: Evaluating the influences of biomass burning during 2006 BASE-ASIA: a regional chemical transport modeling, *Atmos. Chem. Phys.*, 12, 3837–3855, <https://doi.org/10.5194/acp-12-3837-2012>, 2012.
- Golub, G. and Van Loan, C.: *Matrix Computations*, Johns Hopkins Studies in the Mathematical Sciences, Johns Hopkins University Press, Baltimore, London, 1996.
- Gratton, S., Lawless, A. S., and Nichols, N. K.: Approximate Gauss–Newton Methods for Nonlinear Least Squares Problems, *SIAM J. Optimiz.*, 18, 106–132, <https://doi.org/10.1137/050624935>, 2007.
- Gratton, S., Gürol, S., and Toint, P. L.: Preconditioning and globalizing conjugate gradients in dual space for quadratically penalized nonlinear-least squares problems, *Comput. Optim. Appl.*, 54, 1–25, <https://doi.org/10.1007/s10589-012-9478-7>, 2013.
- Grell, G. and Baklanov, A.: Integrated modeling for forecasting weather and air quality: A call for fully coupled approaches, *Atmos. Environ.*, 45, 6845–6851, <https://doi.org/10.1016/j.atmosenv.2011.01.017>, 2011.
- Grell, G., Freitas, S. R., Stuefer, M., and Fast, J.: Inclusion of biomass burning in WRF-Chem: impact of wildfires on weather forecasts, *Atmos. Chem. Phys.*, 11, 5289–5303, <https://doi.org/10.5194/acp-11-5289-2011>, 2011.
- Grell, G. A., Knoche, R., Peckham, S. E., and McKeen, S. A.: Online versus offline air quality modeling on cloud-resolving scales, *Geophys. Res. Lett.*, 31, L16117, <https://doi.org/10.1029/2004GL020175>, 2004.
- Grell, G. A., Peckham, S. E., Schmitz, R., McKeen, S. A., Frost, G., Skamarock, W. C., and Eder, B.: Fully coupled “online” chemistry within the WRF model, *Atmos. Environ.*, 39, 6957–6975, <https://doi.org/10.1016/j.atmosenv.2005.04.027>, 2005 (data available at: <https://ruc.noaa.gov/wrf/wrf-chem/>, last access: 5 June 2017).
- Grieshop, A. P., Lipsky, E. M., Pekney, N. J., Takahama, S., and Robinson, A. L.: Fine particle emission factors from vehicles in a highway tunnel: Effects of fleet composition and season, *Atmos. Environ.*, 40, Supplement 2, 287–298, <https://doi.org/10.1016/j.atmosenv.2006.03.064>, 2006.
- Guerrette, J. J. and Henze, D. K.: Development and application of the WRFPLUS-Chem online chemistry adjoint and WRFDA-Chem assimilation system, *Geosci. Model Dev.*, 8, 1857–1876, <https://doi.org/10.5194/gmd-8-1857-2015>, 2015.
- Halliwell, L. J.: The Lognormal Random Multivariate, in: *Casualty Actuarial Society E-Forum*, Spring 2015, Arlington, Virginia, <http://www.casact.org/pubs/forum/15spforum/Halliwell.pdf> (last access: 9 May 2016), p. 5, 2015.
- Henze, D. K., Seinfeld, J. H., and Shindell, D. T.: Inverse modeling and mapping US air quality influences of inorganic PM_{2.5} precursor emissions using the adjoint of GEOS-Chem, *Atmos. Chem. Phys.*, 9, 5877–5903, <https://doi.org/10.5194/acp-9-5877-2009>, 2009.
- Huang, X.-Y., Xiao, Q., Barker, D. M., Zhang, X., Michalakes, J., Huang, W., Henderson, T., Bray, J., Chen, Y., Ma, Z., Dudhia, J., Guo, Y., Zhang, X., Won, D.-J., Lin, H.-C., and Kuo, Y.-H.: Four-Dimensional Variational Data Assimilation for WRF: Formulation and Preliminary Results, *Mon. Wea. Rev.*, 137, 299–314, <https://doi.org/10.1175/2008MWR2577.1>, 2009.
- Ichoku, C., Kahn, R., and Chin, M.: Satellite contributions to the quantitative characterization of biomass burning for climate modeling, *Atmos. Res.*, 111, 1–28, <https://doi.org/10.1016/j.atmosres.2012.03.007>, 2012.
- Jacob, D. J., Crawford, J. H., Maring, H., Clarke, A. D., Dibb, J. E., Emmons, L. K., Ferrare, R. A., Hostetler, C. A., Russell, P. B., Singh, H. B., Thompson, A. M., Shaw, G. E., McCauley, E., Pederson, J. R., and Fisher, J. A.: The Arctic Research of the Composition of the Troposphere from Aircraft and Satellites (ARCTAS) mission: design, execution, and first results, *Atmos. Chem. Phys.*, 10, 5191–5212, <https://doi.org/10.5194/acp-10-5191-2010>, 2010.
- Janssen, N. A., Gerlofs-Nijland, M. E., Lanki, T., Salonen, R. O., Cassee, F., Hoek, G., Fischer, P., Brunekreef, B., and Krzyzanowski, M.: Health effects of black carbon, World Health Organization, Regional Office for Europe, Copenhagen, http://www.euro.who.int/__data/assets/pdf_file/0004/162535/e96541.pdf (last access: 8 June 2016), 2012.
- Jiang, Z., Jones, D. B. A., Worden, H. M., and Henze, D. K.: Sensitivity of top-down CO source estimates to the modeled vertical structure in atmospheric CO, *Atmos. Chem. Phys.*, 15, 1521–1537, <https://doi.org/10.5194/acp-15-1521-2015>, 2015.
- Jolly, W. M., Cochrane, M. A., Freeborn, P. H., Holden, Z. A., Brown, T. J., Williamson, G. J., and Bowman, D. M. J. S.: Climate-induced variations in global wildfire danger from 1979 to 2013, *Nat. Commun.*, 6, 1–11, <https://doi.org/10.1038/ncomms8537>, 2015.
- Kaiser, J. W., Heil, A., Andreae, M. O., Benedetti, A., Chubarova, N., Jones, L., Morcrette, J.-J., Razinger, M., Schultz, M. G., Suttie, M., and van der Werf, G. R.: Biomass burning emissions estimated with a global fire assimilation system based on observed fire radiative power, *Biogeosciences*, 9, 527–554, <https://doi.org/10.5194/bg-9-527-2012>, 2012.

- Kelley, C.: Iterative Methods for Optimization, *Frontiers in Applied Mathematics*, Society for Industrial and Applied Mathematics, Philadelphia, p. 47, 1999.
- Kim, S.-W., McDonald, B. C., Baidar, S., Brown, S. S., Dube, B., Ferrare, R. A., Frost, G. J., Harley, R. A., Holloway, J. S., Lee, H.-J., McKeen, S. A., Neuman, J. A., Nowak, J. B., Oetjen, H., Ortega, I., Pollack, I. B., Roberts, J. M., Ryerson, T. B., Scarino, A. J., Senff, C. J., Thalman, R., Trainer, M., Volkamer, R., Wagner, N., Washenfelder, R. A., Waxman, E., and Young, C. J.: Modeling the weekly cycle of NO_x and CO emissions and their impacts on O₃ in the Los Angeles–South Coast Air Basin during the CalNex 2010 field campaign: Modeling Weekly Cycle of the LA Air Quality in 2010, *J. Geophys. Res.-Atmos.*, 121, 1340–1360, <https://doi.org/10.1002/2015JD024292>, 2016.
- Lauvaux, T., Miles, N. L., Deng, A., Richardson, S. J., Cambaliza, M. O., Davis, K. J., Gaudet, B., Gurney, K. R., Huang, J., O’Keefe, D., Song, Y., Karion, A., Oda, T., Patarasuk, R., Razliwanov, I., Sarmiento, D., Shepson, P., Sweeney, C., Turnbull, J., and Wu, K.: High-resolution atmospheric inversion of urban CO₂ emissions during the dormant season of the Indianapolis Flux Experiment (INFLUX), *J. Geophys. Res.-Atmos.*, 121, 5213–5236, <https://doi.org/10.1002/2015JD024473>, 2016.
- Lawless, A. S., Gratton, S., and Nichols, N. K.: Approximate iterative methods for variational data assimilation, *Int. J. Numer. Meth. Fl.*, 47, 1129–1135, <https://doi.org/10.1002/flid.851>, 2005.
- Lorenc, A. C.: Optimal nonlinear objective analysis, *Q. J. Roy. Meteor. Soc.*, 114, 205–240, <https://doi.org/10.1002/qj.49711447911>, 1988.
- Malm, W. C., Sisler, J. F., Huffman, D., Eldred, R. A., and Cahill, T. A.: Spatial and seasonal trends in particle concentration and optical extinction in the United States, *J. Geophys. Res.-Atmos.*, 99, 1347–1370, <https://doi.org/10.1029/93JD02916>, 1994 (data available at: <http://views.cira.colostate.edu/fed/DataWizard/Default.aspx>, last access: 5 June 2017).
- Mandel, J., Bergou, E., Gürol, S., Gratton, S., and Kasanický, I.: Hybrid Levenberg-Marquardt and weak-constraint ensemble Kalman smoother method, *Nonlin. Processes Geophys.*, 23, 59–73, <https://doi.org/10.5194/npg-23-59-2016>, 2016.
- Mao, Y. H., Li, Q. B., Zhang, L., Chen, Y., Randerson, J. T., Chen, D., and Liou, K. N.: Biomass burning contribution to black carbon in the Western United States Mountain Ranges, *Atmos. Chem. Phys.*, 11, 11253–11266, <https://doi.org/10.5194/acp-11-11253-2011>, 2011.
- Mao, Y. H., Li, Q. B., Henze, D. K., Jiang, Z., Jones, D. B. A., Kopacz, M., He, C., Qi, L., Gao, M., Hao, W.-M., and Liou, K.-N.: Estimates of black carbon emissions in the western United States using the GEOS-Chem adjoint model, *Atmos. Chem. Phys.*, 15, 7685–7702, <https://doi.org/10.5194/acp-15-7685-2015>, 2015.
- McDonald, B. C., Goldstein, A. H., and Harley, R. A.: Long-Term Trends in California Mobile Source Emissions and Ambient Concentrations of Black Carbon and Organic Aerosol, *Environ. Sci. Technol.*, 49, 5178–5188, <https://doi.org/10.1021/es505912b>, 2015.
- Meirink, J. F., Bergamaschi, P., and Krol, M. C.: Four-dimensional variational data assimilation for inverse modelling of atmospheric methane emissions: method and comparison with synthesis inversion, *Atmos. Chem. Phys.*, 8, 6341–6353, <https://doi.org/10.5194/acp-8-6341-2008>, 2008.
- Müller, J.-F. and Stavrakou, T.: Inversion of CO and NO_x emissions using the adjoint of the IMAGES model, *Atmos. Chem. Phys.*, 5, 1157–1186, <https://doi.org/10.5194/acp-5-1157-2005>, 2005.
- NASA: MCD14ML MODIS Active Fire Detections, available at: <https://earthdata.nasa.gov/active-fire-data#tab-content-6>, last access: 18 December 2014.
- Peischl, J., Ryerson, T. B., Brioude, J., Aikin, K. C., Andrews, A. E., Atlas, E., Blake, D., Daube, B. C., de Gouw, J. A., Dlugokencky, E., Frost, G. J., Gentner, D. R., Gilman, J. B., Goldstein, A. H., Harley, R. A., Holloway, J. S., Kofler, J., Kuster, W. C., Lang, P. M., Novelli, P. C., Santoni, G. W., Trainer, M., Wofsy, S. C., and Parrish, D. D.: Quantifying sources of methane using light alkanes in the Los Angeles basin, California, *J. Geophys. Res.-Atmos.*, 118, 4974–4990, <https://doi.org/10.1002/jgrd.50413>, 2013.
- Pleim, J. E.: A Simple, Efficient Solution of Flux–Profile Relationships in the Atmospheric Surface Layer, *J. Appl. Meteorol. Clim.*, 45, 341–347, <https://doi.org/10.1175/JAM2339.1>, 2006.
- Pleim, J. E.: A Combined Local and Nonlocal Closure Model for the Atmospheric Boundary Layer. Part II: Application and Evaluation in a Mesoscale Meteorological Model, *J. Appl. Meteorol. Clim.*, 46, 1396–1409, <https://doi.org/10.1175/JAM2534.1>, 2007a.
- Pleim, J. E.: A Combined Local and Nonlocal Closure Model for the Atmospheric Boundary Layer. Part I: Model Description and Testing, *J. Appl. Meteorol. Clim.*, 46, 1383–1395, <https://doi.org/10.1175/JAM2539.1>, 2007b.
- Pleim, J. E. and Gilliam, R.: An Indirect Data Assimilation Scheme for Deep Soil Temperature in the Pleim–Xiu Land Surface Model, *J. Appl. Meteorol. Clim.*, 48, 1362–1376, <https://doi.org/10.1175/2009JAMC2053.1>, 2009.
- Pleim, J. E. and Xiu, A.: Development of a land surface model. Part II: Data assimilation, *J. Appl. Meteorol.*, 42, 1811–1822, [https://doi.org/10.1175/1520-0450\(2003\)042<1811:DOALSM>2.0.CO;2](https://doi.org/10.1175/1520-0450(2003)042<1811:DOALSM>2.0.CO;2), 2003.
- Purser, R. J. and Huang, H.-L.: Estimating Effective Data Density in a Satellite Retrieval or an Objective Analysis, *J. Appl. Meteorol.*, 32, 1092–1107, [https://doi.org/10.1175/1520-0450\(1993\)032<1092:EEDDIA>2.0.CO;2](https://doi.org/10.1175/1520-0450(1993)032<1092:EEDDIA>2.0.CO;2), 1993.
- Reff, A., Bhawe, P. V., Simon, H., Pace, T. G., Pouliot, G. A., Mobley, J. D., and Houyoux, M.: Emissions Inventory of PM_{2.5} Trace Elements across the United States, *Environ. Sci. Technol.*, 43, 5790–5796, <https://doi.org/10.1021/es802930x>, 2009.
- Reid, J. S., Hyer, E. J., Prins, E. M., Westphal, D. L., Zhang, J., Wang, J., Christopher, S. A., Curtis, C. A., Schmidt, C. C., Eleuterio, D. P., Richardson, K. A., and Hoffman, J. P.: Global Monitoring and Forecasting of Biomass-Burning Smoke: Description of and Lessons From the Fire Locating and Modeling of Burning Emissions (FLAMBE) Program, *IEEE J. Sel. Top. Appl.*, 2, 144–162, <https://doi.org/10.1109/JSTARS.2009.2027443>, 2009.
- Rodgers, C. D.: Information content and optimization of high-spectral-resolution measurements, in: *Proc. SPIE*, vol. 2830, 136–147, <https://doi.org/10.1117/12.256110>, 1996.
- Sahu, L. K., Kondo, Y., Moteki, N., Takegawa, N., Zhao, Y., Cubison, M. J., Jimenez, J. L., Vay, S., Diskin, G. S., Wisthaler, A., Mikoviny, T., Huey, L. G., Weinheimer, A. J., and Knapp, D. J.: Emission characteristics of black carbon in anthropogenic and biomass burning plumes over California during ARCTAS-CARB 2008, *J. Geophys. Res.*, 117, D16302,

- <https://doi.org/10.1029/2011JD017401>, 2012 (data available at: <https://www-air.larc.nasa.gov/cgi-bin/ArcView/arctas#KONDO.YUTAKA/>, last access: 5 June 2017).
- Saide, P. E., Peterson, D. A., da Silva, A., Anderson, B., Ziemba, L. D., Diskin, G., Sachse, G., Hair, J., Butler, C., Fenn, M., Jimenez, J. L., Campuzano-Jost, P., Perring, A. E., Schwarz, J. P., Markovic, M. Z., Russell, P., Redemann, J., Shinzuka, Y., Streets, D. G., Yan, F., Dibb, J., Yokelson, R., Toon, O. B., Hyer, E., and Carmichael, G. R.: Revealing important nocturnal and day-to-day variations in fire smoke emissions through a multiplatform inversion, *Geophys. Res. Lett.*, 42, 3609–3618, <https://doi.org/10.1002/2015GL063737>, 2015.
- Song, H., Edwards, C. A., Moore, A. M., and Fiechter, J.: Data assimilation in a coupled physical–biogeochemical model of the California Current System using an incremental lognormal 4-dimensional variational approach: Part 1 – Model formulation and biological data assimilation twin experiments, *Ocean Model.*, 106, 131–145, <https://doi.org/10.1016/j.ocemod.2016.04.001>, 2016.
- Spracklen, D. V., Mickley, L. J., Logan, J. A., Hudman, R. C., Yevich, R., Flannigan, M. D., and Westerling, A. L.: Impacts of climate change from 2000 to 2050 on wildfire activity and carbonaceous aerosol concentrations in the western United States, *J. Geophys. Res.*, 114, D20301, <https://doi.org/10.1029/2008JD010966>, 2009.
- Strand, T. M., Larkin, N., Craig, K. J., Raffuse, S., Sullivan, D., Solomon, R., Rorig, M., Wheeler, N., and Pryden, D.: Analyses of BlueSky Gateway PM_{2.5} predictions during the 2007 southern and 2008 northern California fires: PM_{2.5} PREDICTIONS DURING LARGE WILDFIRES, *J. Geophys. Res.-Atmos.*, 117, D17301, <https://doi.org/10.1029/2012JD017627>, 2012.
- Streets, D. G., Bond, T. C., Carmichael, G. R., Fernandes, S. D., Fu, Q., He, D., Klimont, Z., Nelson, S. M., Tsai, N. Y., Wang, M. Q., Woo, J.-H., and Yarber, K. F.: An inventory of gaseous and primary aerosol emissions in Asia in the year 2000, *J. Geophys. Res.-Atmos.*, 108, GTE30/1–GTE30/23, <https://doi.org/10.1029/2002JD003093>, 2003.
- Tarantola, A.: *Inverse Problem Theory and Methods for Model Parameter Estimation*, Other Titles in Applied Mathematics, Society for Industrial and Applied Mathematics, Philadelphia, 74–75, <https://doi.org/10.1137/1.9780898717921>, 2005.
- Thacker, W. C.: The role of the Hessian matrix in fitting models to measurements, *J. Geophys. Res.-Oceans*, 94, 6177–6196, <https://doi.org/10.1029/JC094iC05p06177>, 1989.
- Tshimanga, J., Gratton, S., Weaver, A. T., and Sartenaer, A.: Limited-memory preconditioners, with application to incremental four-dimensional variational data assimilation, *Q. J. Roy. Meteor. Soc.*, 134, 751–769, <https://doi.org/10.1002/qj.228>, 2008.
- van der Werf, G. R., Randerson, J. T., Giglio, L., Collatz, G. J., Mu, M., Kasibhatla, P. S., Morton, D. C., DeFries, R. S., Jin, Y., and van Leeuwen, T. T.: Global fire emissions and the contribution of deforestation, savanna, forest, agricultural, and peat fires (1997–2009), *Atmos. Chem. Phys.*, 10, 11707–11735, <https://doi.org/10.5194/acp-10-11707-2010>, 2010.
- Wahba, G.: Design Criteria and Eigensequence Plots for Satellite-Computed Tomography, *J. Atmos. Ocean. Tech.*, 2, 125–132, [https://doi.org/10.1175/1520-0426\(1985\)002<0125:DCAEPF>2.0.CO;2](https://doi.org/10.1175/1520-0426(1985)002<0125:DCAEPF>2.0.CO;2), 1985.
- Wecht, K. J., Jacob, D. J., Sulprizio, M. P., Santoni, G. W., Wofsy, S. C., Parker, R., Bösch, H., and Worden, J.: Spatially resolving methane emissions in California: constraints from the CalNex aircraft campaign and from present (GOSAT, TES) and future (TROPOMI, geostationary) satellite observations, *Atmos. Chem. Phys.*, 14, 8173–8184, <https://doi.org/10.5194/acp-14-8173-2014>, 2014.
- Wesely, M. L.: Parameterization of surface resistances to gaseous dry deposition in regional-scale numerical models, *Atmos. Environ.*, 23, 1293–1304, [https://doi.org/10.1016/0004-6981\(89\)90153-4](https://doi.org/10.1016/0004-6981(89)90153-4), 1989.
- Wiedinmyer, C., Quayle, B., Geron, C., Belote, A., McKenzie, D., Zhang, X., O'Neill, S., and Wynne, K. K.: Estimating emissions from fires in North America for air quality modeling, *Atmos. Environ.*, 40, 3419–3432, <https://doi.org/10.1016/j.atmosenv.2006.02.010>, 2006 (data available at: <http://bai.acom.ucar.edu/Data/fire/>, last access: 5 June 2017).
- Wiedinmyer, C., Akagi, S. K., Yokelson, R. J., Emmons, L. K., Al-Saadi, J. A., Orlando, J. J., and Soja, A. J.: The Fire INventory from NCAR (FINN): a high resolution global model to estimate the emissions from open burning, *Geosci. Model Dev.*, 4, 625–641, <https://doi.org/10.5194/gmd-4-625-2011>, 2011 (data available at: <http://bai.acom.ucar.edu/Data/fire/>, last access: 5 June 2017).
- WRAP: 2002 Fire Emission Inventory for the WRAP Region – Phase II, Tech. Rep. Project No. 178-6, Prepared by Air Sciences, Inc., <https://www.wrapair.org/forums/fejftasks/FEJFtask7PhaseII.html> (last access: 2 April 2016), 2005.
- Wu, J., Winer, A. M., and Delfino, R. J.: Exposure assessment of particulate matter air pollution before, during, and after the 2003 Southern California wildfires, *Atmos. Environ.*, 40, 3333–3348, <https://doi.org/10.1016/j.atmosenv.2006.01.056>, 2006.
- Xiu, A. and Pleim, J. E.: Development of a land surface model. Part I: Application in a mesoscale meteorological model, *J. Appl. Meteorol.*, 40, 192–209, [https://doi.org/10.1175/1520-0450\(2001\)040<0192:DOALSM>2.0.CO;2](https://doi.org/10.1175/1520-0450(2001)040<0192:DOALSM>2.0.CO;2), 2001.
- Yang, E.-G., Kim, H. M., Kim, J., and Kay, J. K.: Effect of Observation Network Design on Meteorological Forecasts of Asian Dust Events, *Mon. Weather Rev.*, 142, 4679–4695, <https://doi.org/10.1175/MWR-D-14-00080.1>, 2014.
- Yelverton, T. L., Hays, M. D., Gullett, B. K., and Linak, W. P.: Black Carbon Measurements of Flame-Generated Soot as Determined by Optical, Thermal-Optical, Direct Absorption, and Laser Incandescence Methods, *Environ. Eng. Sci.*, 31, 209–215, <https://doi.org/10.1089/ees.2014.0038>, 2014.
- Zhang, F., Wang, J., Ichoku, C., Hyer, E. J., Yang, Z., Ge, C., Su, S., Zhang, X., Kondragunta, S., Kaiser, J. W., Wiedinmyer, C., and da Silva, A.: Sensitivity of mesoscale modeling of smoke direct radiative effect to the emission inventory: a case study in northern sub-Saharan African region, *Environ. Res. Lett.*, 9, 075002, <https://doi.org/10.1088/1748-9326/9/7/075002>, 2014.
- Zhang, X., Kondragunta, S., Ram, J., Schmidt, C., and Huang, H.-C.: Near-real-time global biomass burning emissions product from geostationary satellite constellation: GLOBAL BIOMASS BURNING EMISSIONS, *J. Geophys. Res.-Atmos.*, 117, D14201, <https://doi.org/10.1029/2012JD017459>, 2012.

Zhang, X., Huang, X.-Y., and Pan, N.: Development of the Upgraded Tangent Linear and Adjoint of the Weather Research and Forecasting (WRF) Model, *J. Atmos. Ocean. Tech.*, 30, 1180–1188, <https://doi.org/10.1175/JTECH-D-12-00213.1>, 2013.

Zhang, X., Huang, X.-Y., Liu, J., Poterjoy, J., Weng, Y., Zhang, F., and Wang, H.: Development of an Efficient Regional Four-Dimensional Variational Data Assimilation System for WRF, *J. Atmos. Ocean. Tech.*, 31, 2777–2794, <https://doi.org/10.1175/JTECH-D-13-00076.1>, 2014.